Stem Cell Reports
Article

ISSCR

OPEN ACCESS

Human motor units in microfluidic devices are impaired by *FUS* mutations and improved by HDAC6 inhibition

Katarina Stoklund Dittlau,[1,2] Emily N. Krasnow,[1,2] Laura Fumagalli,[1,2] Tijs Vandoorne,[1,2] Pieter Baatsen,[3,4] Axelle Kerstens,[3,4] Giorgia Giacomazzi,[5] Benjamin Pavie,[3,4] Elisabeth Rossaert,[1,2] Jimmy Beckers,[1,2] Maurilio Sampaolesi,[5] Philip Van Damme,[1,2,6] and Ludo Van Den Bosch[1,2,*]

[1]KU Leuven – University of Leuven, Department of Neurosciences, Experimental Neurology, and Leuven Brain Institute, Leuven, Belgium
[2]VIB, Center for Brain & Disease Research, Laboratory of Neurobiology, Leuven, Belgium
[3]VIB, Center for Brain & Disease Research, Research Group Molecular Neurobiology, Leuven, Belgium
[4]KU Leuven – University of Leuven, VIB Bio Imaging Core, Leuven, Belgium
[5]KU Leuven – University of Leuven, Department of Development and Regeneration, Stem Cell and Developmental Biology, Leuven, Belgium
[6]University Hospitals Leuven, Department of Neurology, Leuven, Belgium
*Correspondence: ludo.vandenbosch@kuleuven.be
https://doi.org/10.1016/j.stemcr.2021.03.029

SUMMARY

Neuromuscular junctions (NMJs) ensure communication between motor neurons (MNs) and muscle; however, in MN disorders, such as amyotrophic lateral sclerosis (ALS), NMJs degenerate resulting in muscle atrophy. The aim of this study was to establish a versatile and reproducible *in vitro* model of a human motor unit to investigate the effects of ALS-causing mutations. Therefore, we generated a co-culture of human induced pluripotent stem cell (iPSC)-derived MNs and human primary mesoangioblast-derived myotubes in microfluidic devices. A chemotactic and volumetric gradient facilitated the growth of MN neurites through microgrooves resulting in the interaction with myotubes and the formation of NMJs. We observed that ALS-causing *FUS* mutations resulted in reduced neurite outgrowth as well as an impaired neurite regrowth upon axotomy. NMJ numbers were likewise reduced in the *FUS*-ALS model. Interestingly, the selective HDAC6 inhibitor, Tubastatin A, improved the neurite outgrowth, regrowth, and NMJ morphology, prompting HDAC6 inhibition as a potential therapeutic strategy for ALS.

INTRODUCTION

Neuromuscular junctions (NMJs) are specialized synapses, which are crucial for the communication between spinal lower motor neurons (MNs) and skeletal muscle (Plomp 2018). NMJs become vulnerable in neurodegenerative diseases, such as amyotrophic lateral sclerosis (ALS), where the degeneration of NMJs results in muscle weakness and atrophy, ultimately causing respiratory insufficiency and death (Dadon-Nachum et al., 2010; Murray et al., 2010). There is ample evidence that the disconnection of the motor axon from the muscle is the first step in the disease process of ALS (Fischer et al., 2004; Martineau et al., 2018), making it an important mechanism to study. Initially, the MN will compensate for this retraction by axonal sprouting and collateral reinnervation. However, when the disease progresses, this compensation fails and the MN eventually dies, a phenomenon defined as the "dying-back" mechanism (Robberecht and Philips, 2013). Symptoms in patients start to occur when large populations of MNs are affected, resulting in weakness of muscle groups. MNs have very long axons, which makes them more susceptible to this dying-back mechanism compared with other neurons. This partially explains the selective vulnerability in ALS pathogenesis, and evidence of dying back and loss of NMJs has been reported in several ALS-mouse models and in patients (Fischer et al., 2004; Martineau et al., 2018; Nair et al., 2010; So et al., 2018; Tallon et al., 2016; Walker et al., 2015).

To further study the NMJs and their relation to ALS, it is beneficial to have a standardized, human cell-derived model of these NMJs *in vitro*, for which co-culturing of MNs and skeletal muscle is required. Co-cultures of these highly specialized cell types in single compartments have been developed using both human and animal cells and, in some studies, functional NMJs were established (Demestre et al., 2015; Guo et al., 2011; Lin et al., 2019; Puttonen et al., 2015; Umbach et al., 2012). However, such models are unable to account for the unique culture microenvironments occupied by cell-specific domains of MNs and muscle fibers (de Jongh et al., 2021; Millet and Gillette, 2012). The use of "Campenot" chambers (Campenot 1977) and microfluidic devices offers the opportunity to overcome this problem (Bellmann et al., 2019; Mills et al., 2018; Osaki et al., 2018a; Santhanam et al., 2018; Southam et al., 2013; Zahavi et al., 2015). The fluidically isolated compartments, between which only neurites can grow, not only allow for maintenance of cell-type-specific microenvironments, but also allow for isolation of subcellular compartments, such as the distal and the proximal part of the axon, for region-specific analyses (Naumann et al., 2018; Nijssen et al., 2018; Taylor et al., 2005).

While the development of customized microfluidic platforms (Bellmann et al., 2019; Osaki et al., 2018b) has

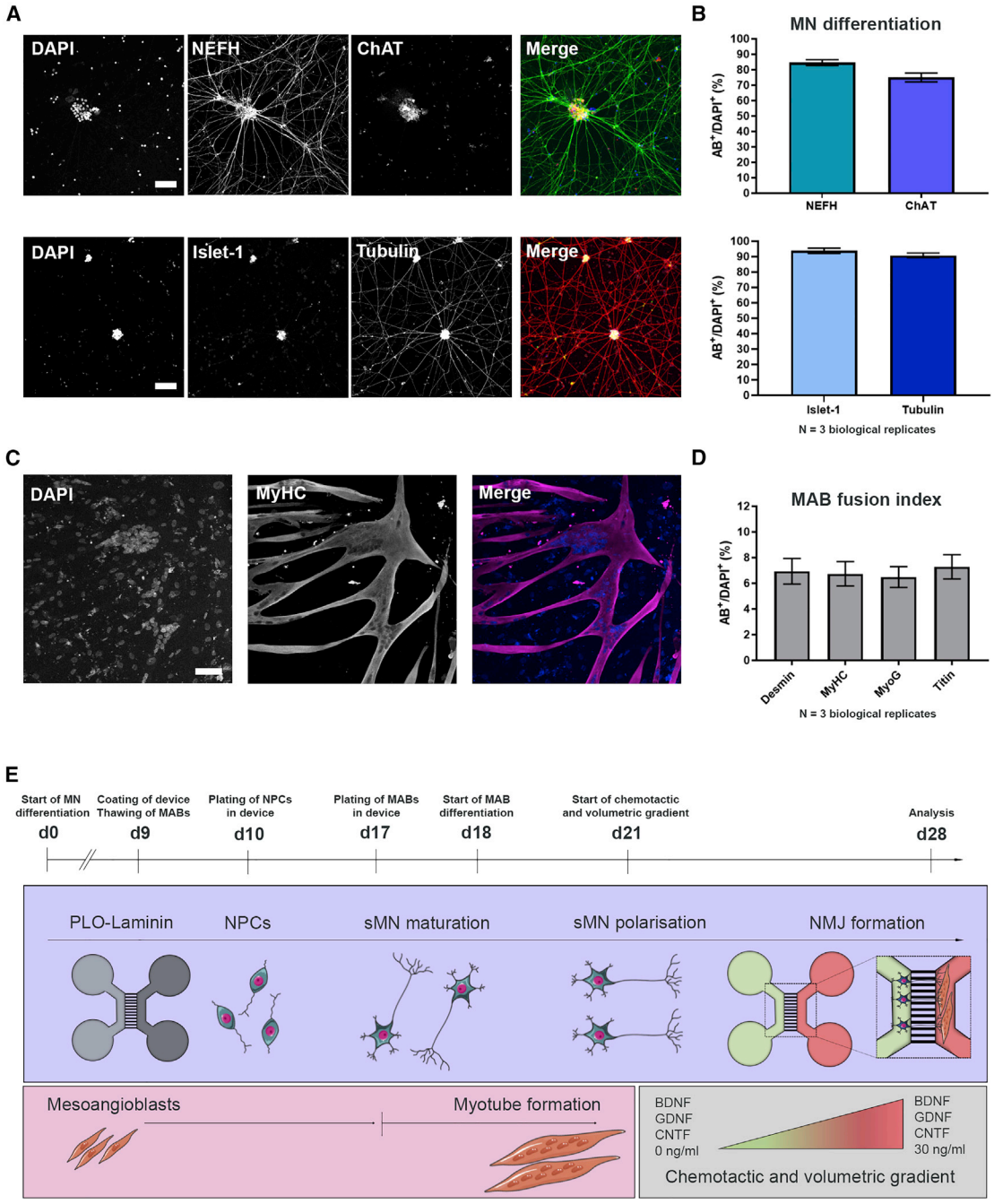

Figure 1. Characterization of monocultures and overview of NMJ protocol

(A) Confocal images of MNs stained with MN markers neurofilament heavy chain (NEFH), choline acetyltransferase (ChAT), and Islet-1, as well as the pan-neuronal marker βIII-tubulin (Tubulin) at day 28 of MN differentiation. Nuclei stained with DAPI. Scale bars, 75 μm.

(B) Number of cells positive for MN and pan-neuronal markers (AB^+). Mean ± SEM of three biological replicates.

(C) Confocal images of myotube heavy chain (MyHC)-positive myotubes 10 days after initiation of differentiation. Scale bar, 75 μm.

(D) Quantification of mesoangioblast (MAB) fusion into multinucleated myotubes (fusion index) with myotube markers desmin, MyHC, myogenin (MyoG) or titin. Mean ± SEM of three biological replicates.

(E) Schematic overview of co-culture protocol and differentiation timeline (days 0–28). Day 0 (d0), differentiation of iPSCs into MN. Day 9 (d9), microfluidic devices are coated with poly-L-ornithine (PLO) and laminin, and MABs are thawed for expansion. Day 10 (d10), MN-NPCs are plated on one side (light gray) of the device. Day 17 (d17), MABs are seeded in the opposite side of the device (dark gray). Myotube

(legend continued on next page)

significantly improved the potential for disease modeling, a standardized accessible method for the formation of human NMJs *in vitro* is lacking. Therefore, we aimed to develop a human-derived system, which combines commercially available microfluidic devices, induced pluripotent stem cell (iPSC)-derived MNs, and mesoangioblasts (MAB)-derived myotubes to generate and study functional human NMJs in a compartmentalized system. With the supplementation of agrin and laminin (A/L), we increased the clustering of nicotinic acetylcholine receptors (AChRs), the outgrowth of neurites and the formation of NMJs. Using this model, we discovered a compromised outgrowth and regrowth after axotomy of MN neurites, as well as an impairment in NMJ numbers in ALS-*FUS* mutant co-cultures in comparison with their CRISPR-Cas9 gene-edited isogenic controls. Interestingly, we could improve these phenotypes by treating with the selective histone deacetylase 6 (HDAC6) inhibitor, Tubastatin A (TubA). Our findings show that this *in vitro* model is a valuable tool to assess human NMJ physiology in health and disease.

RESULTS

Generation of human iPSC-derived MNs and MAB-derived myotubes

To generate human NMJs *in vitro*, we made use of human iPSCs (hiPSCs) and human primary MABs. MABs are vessel-associated mesenchymal stem cells, which are isolated from adult skeletal muscle tissue (Dellavalle et al., 2007; Rotini et al., 2018; Tonlorenzi et al., 2007). MABs were expanded and subsequently differentiated into myotubes over a 10-day period, while hiPSCs were differentiated into MNs via a 28-day protocol (Guo et al., 2017). MN differentiation efficiency and MAB fusion index were evaluated using immunocytochemistry (ICC). At day 28 of MN differentiation, the hiPSC-derived MNs stained positive for MN-specific markers neurofilament heavy chain (NEFH), choline acetyltransferase, and Islet-1, in addition to the pan-neuronal marker βIII-tubulin (Figures 1A and 1B), similar to previous studies utilizing the same MN differentiation protocol (Guo et al., 2017; Vandoorne et al., 2019). After 10 days of differentiation, the human MAB-derived multinucleated myotubes stained positive for specific muscle markers (Figures 1C, 1D, and S1).

NMJs spontaneously form in a MN-myotube microfluidic co-culture system

To generate NMJs through co-culturing of MNs and MABs, we utilized two types of Xona Microfluidics devices (SND75 and XC150). To ensure compartmentalization, MN-neural progenitor cells (NPCs) were plated at day 10 of MN differentiation on one side of the device (Figure 1E, light gray compartment) and allowed to differentiate for 1 week in the device, before MABs were plated at day 17 of MN differentiation on the other side of the fluidically isolated device (Figures 1E, dark gray compartment and S1). The difference in plating time was conducted to ensure an efficient co-culture between maturing MNs and fusing myotubes, to make full use of the culture window in which MAB-derived myotubes are viable.

On day 21 of MN differentiation, a chemotactic growth factor and volumetric gradient was implemented to induce the migration of MN axons (Figure 1E, green compartment) through the microgrooves to the compartment containing myotubes (Figure 1E, red compartment). Due to these gradients, a larger proportion of axons migrated through the microgrooves from the MN compartment toward the myotube compartment (Figure 2A), where they were able to connect with clusters of α-bungarotoxin (Btx)-positive AChRs expressed on myotubes. AChRs represent an important guidance cue for MN axons and hence NMJ formation *in vivo* (Burden et al., 2018) and we could indeed observe interactions of MN neurites and AChR clusters on myotubes indicative of the formation of NMJ-like structures (referred to as NMJs from here on) (Figures 2B and 2C). However, only a limited number of AChR clusters and hence NMJs were identified in each culture.

Agrin and laminin stimulate neurite outgrowth and NMJ formation

To increase the NMJ numbers in our model, we tested whether supplementing the myotube culture medium with A/L had an effect, as these compounds have been shown to increase the AChR clustering at the sarcolemma as well as to enhance NMJ formation (Afshar Bakooshli et al., 2019; Burkin et al., 2000; Zhang et al., 2016). AChR clustering on cultured myotubes is independent of neuronal presence (Kummer et al., 2004; Osseni et al., 2020), so, to investigate the effect on human primary MABs-derived myotubes, we quantified AChR clustering with and without these compounds (Figure S2). Our data

differentiation is initiated (d18). Day 21 (d21), a volumetric and chemotactic gradient of neurotrophic factors (BDNF, GDNF and CNTF) is implemented to facilitate polarized growth of spinal MNs (sMN) through the microgrooves toward the myotubes to initiate the formation of NMJs (d28). Cell illustrations were modified from Smart Servier Medical Art licensed under a Creative Commons Attribution 3.0 Unported License (https://creativecommons.org/licenses/by/3.0/).
See also Figure S1.

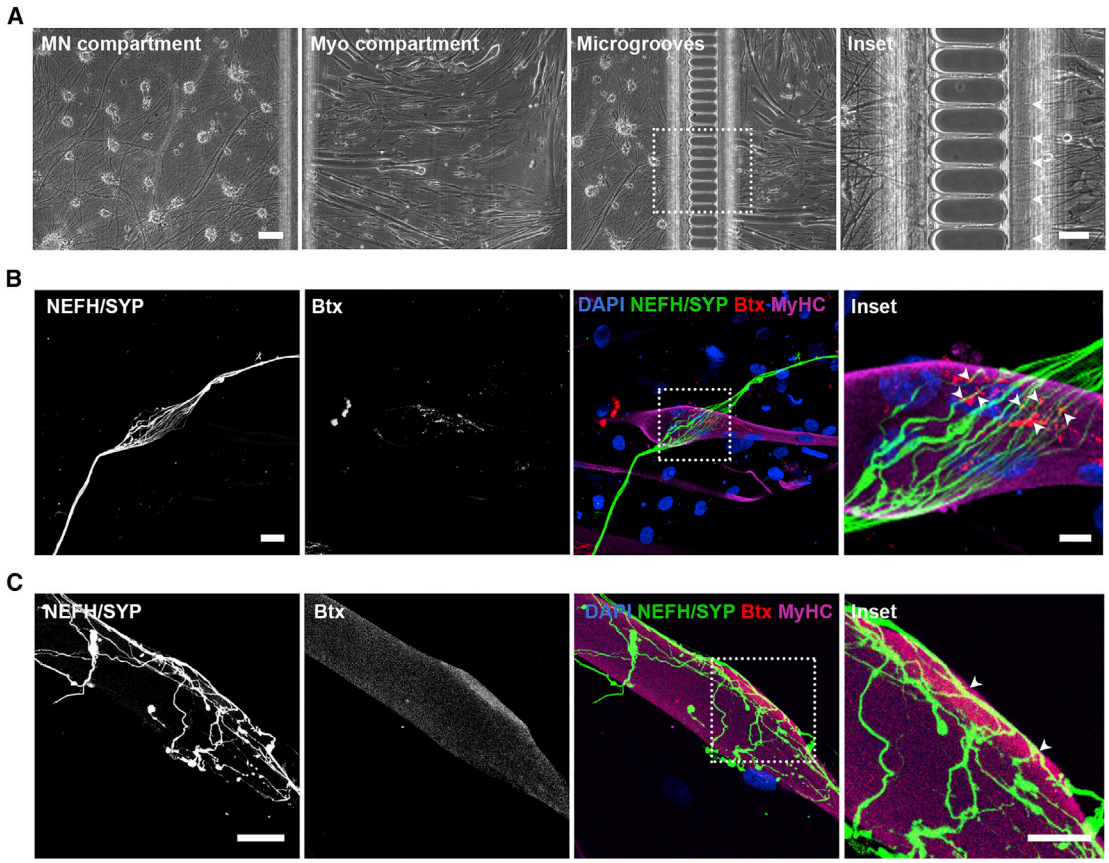

Figure 2. Co-culturing of MNs and myotubes in microfluidic devices leads to NMJ formation

(A) Bright-field micrographs of MN and myotube (Myo) compartments in the XC150 device on day 28. Insets: magnification of axonal migration through microgrooves (arrowheads). Scale bars, 100 μm and 50 μm (insets).

(B and C) Confocal micrograph of NMJ formation are shown as co-localization of presynaptic marker synaptophysin (SYP) and acetylcholine receptor marker α-bungarotoxin (Btx) on MyHC-labeled myotubes. Insets: magnification of co-localizations (arrowheads). Scale bars, 25 μm and 10 μm (insets).

showed an increase in AChR clusters per myotube with A/L in comparison with untreated controls (Figure S2C). A/L supplementation did not affect the ability of MABs to fuse into myotubes (Figure S1).

NMJs were identified through co-localization of distal neurites (NEFH and synaptophysin) with Btx-positive AChRs on MyHC-labeled myotubes and the number of interactions was normalized to the number of myotubes. The NMJs either appeared rudimentary and circular as single contact point NMJs (Figures 3A and S2D), or elongated with broad, flat, irregular multiple contact point NMJs (Figures 3B and S2E). In most cases, contacts between axons and myotubes did not produce distinct axon termination in endplate formation as seen *in vivo* but rather revealed a continuation of axonal growth after embedment into myotubes (Figure 3B). No obvious morphological differences in size, shape, or embedment form were observed immunocytochemically between controls and conditions with A/L (Figures 3 and S2). However, addition of A/L doubled the total number of NMJs per myotube in comparison with control devices (Figure 3C). A/L also increased the number of multiple contact point NMJs in comparison with single contact point NMJs (Figure 3D). Scanning electron microscopy (SEM) showed neurite embedment into the surface of myotubes (Figures 3E and 3F) in line with our ICC observations. In addition, we observed larger, elongated NMJs with A/L compared with untreated controls, further confirming the beneficial effect of these compounds.

As A/L are signaling molecules important for neurite guidance, we investigated whether these supplements have an effect on neurite outgrowth in addition to NMJ formation. To quantify the difference, we acquired tile scan images of the myotube compartment and isolated the neurites (Figure S3). The images were converted to a mask and analyzed with a linear Scholl analysis script similar to a previously published method (Jocher et al., 2018) (Figures S3A

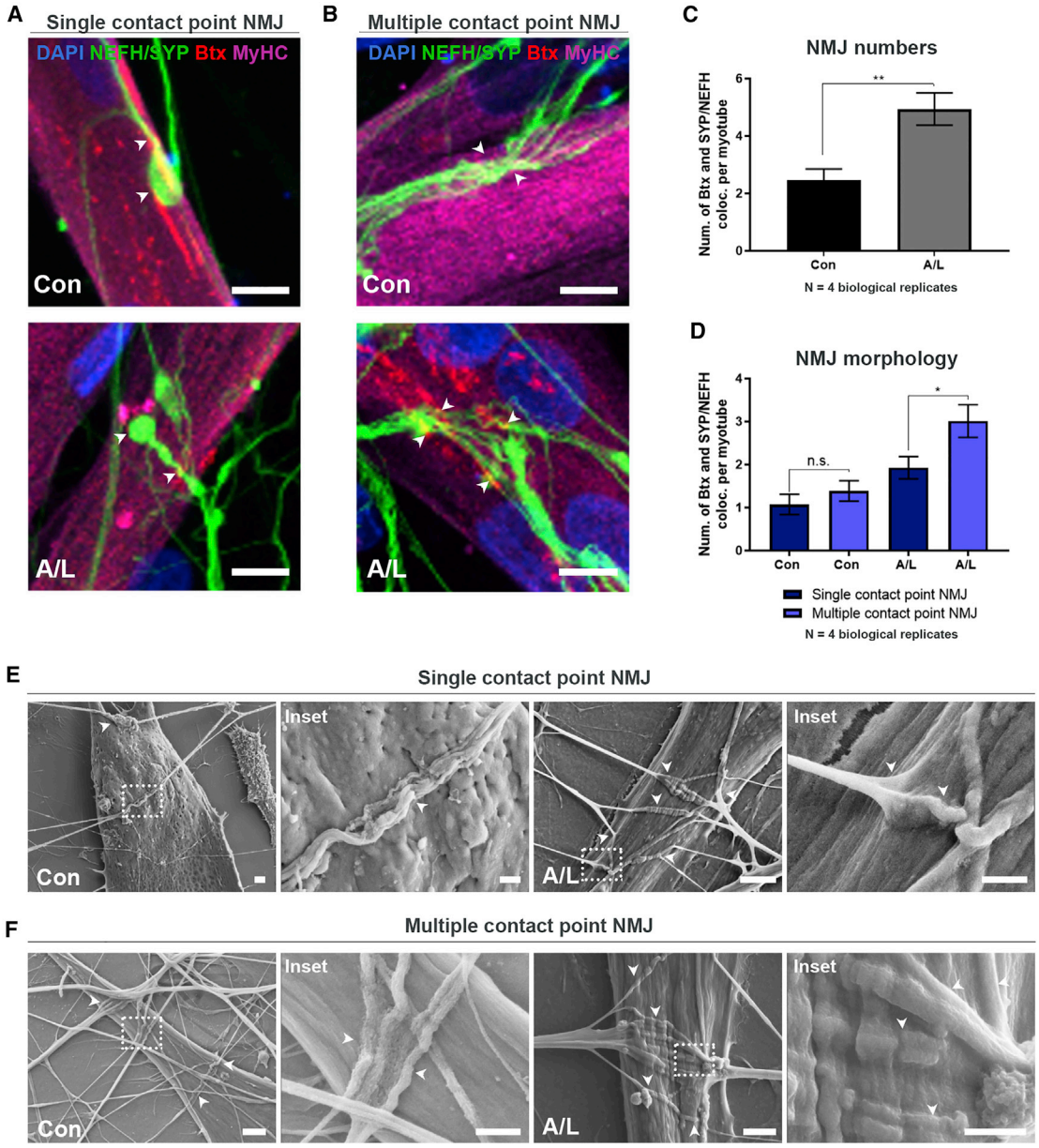

Figure 3. Agrin and laminin improve NMJ formation in microfluidic devices

(A and B) Confocal micrographs of NMJs in agrin (0.01 μg/mL)- and laminin (20 μg/mL)-supplemented (A/L) and untreated (Con) conditions on day 28 in XC150 devices. Single contact point NMJs (A). Multiple contact point NMJs (B). Scale bars, 10 μm. Arrowheads: Btx-SYP/NEFH co-localizations.

(C) Number of Btx and SYP/NEFH co-localizations per myotube.

(D) Quantifications of NMJ single and multiple contact point morphology.

(E and F) Representative scanning electron microscopy (SEM) images of NMJ formation in SND75 devices on day 28 in A/L-supplemented and control conditions. Single contact point NMJs (E). Multiple contact point NMJs (F). Insets: magnifications of NMJ (arrowheads). Scale bars, 2 μm and 1 μm (insets). (C) Unpaired t test. (D) One-way ANOVA with Tukey's multiple comparisons test. Mean ± SEM of four biological replicates. *$p < 0.05$, **$p < 0.01$.

See also Figures S2 and S3.

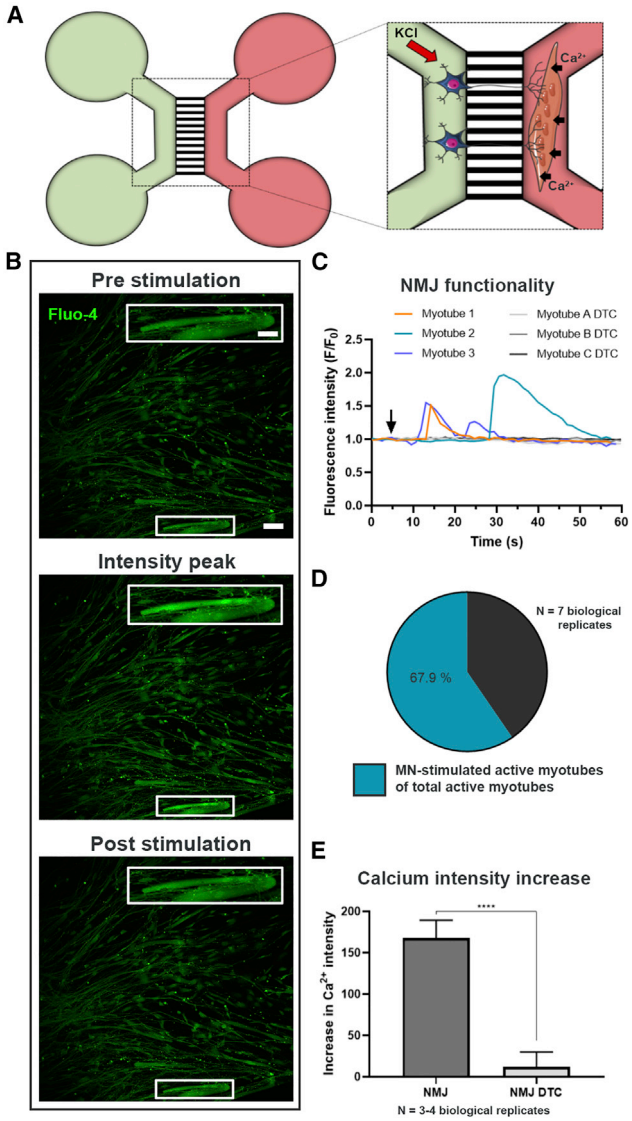

Figure 4. *In vitro* NMJs are functionally active

(A) Schematic overview of transient fluorescent Ca^{2+} imaging in XC150 devices on day 28. MN compartment (green) is stimulated with 50 mM KCl, which initiates an intracellular response through MN axons evoking an increase in Ca^{2+} influx in the Fluo-4-loaded myotubes (red compartment). Cell illustrations are modified from Smart Servier Medical Art licensed under a Creative Commons Attribution 3.0 Unported License (https://creativecommons.org/licenses/by/3.0/).

(B) Fluorescent micrograph examples of before, during, and after stimulation depicting a wave of increase in intracellular Ca^{2+} in myotubes upon MN stimulation. Inset shows a magnification of an innervated active myotube. Scale bars, 100 μm and 200 μm (insets).

(C) Representative Ca^{2+} influx curves in myotubes after KCl activation (arrow) of MNs before (myotube 1–3) and after 10 min treatment with NMJ blocker tubocurarine (myotube A-C DTC).

(D) Ratio of MN-stimulated active myotubes to directly KCl-activated myotubes.

(E) Effect of DTC on the intensity fluorescent increase due to Ca^{2+} influx induced by KCl increase in the MN compartment. Mean ± SEM of three to four biological replicates. Mann-Whitney test. ****$p < 0.0001$.

See also Figure S4.

and S3B). The Scholl analysis creates an intersection line every 50 μm, and the number of neurite pixels per intersection was quantified (Figure S3C). Due to the high density of neurites, which grow through the microgrooves in thick bundles, we omitted the first intersection at 50 μm distance from the microgroove exit. The initial exponential increase in pixel intersections correlated with the "debundling" and spreading of neurites post microgroove crossing (Figure S3C). Interestingly, we found an increase in neurite outgrowth due to A/L treatment.

Taken together, these results demonstrate the formation of human NMJs in our *in vitro* system. Supplementation of A/L promoted the outgrowth of neurites and increased the total number of NMJs per myotube as well as the contact areas between branching MN axons and myotubes further enhancing the embedment.

Human *in vitro* NMJs are functional through MN stimulation

To evaluate whether the NMJs were functional, we performed live-cell Ca^{2+} imaging (Figure 4). MN somas and proximal axons were depolarized using 50 mM KCl and a subsequent increase in Ca^{2+} influx in the myotubes preloaded with the Ca^{2+}-sensitive Fluo-4 dye was measured (Figure 4A). The fluidic isolation of the compartments in the microfluidic device ensured no direct contact between the high KCl solution and the myotubes (Figure S4A). Stimulation of MNs resulted in Ca^{2+} transient waves in the MN-innervated myotubes, indicating a functional connection through NMJ formation (Figures 4B and 4C).

To differentiate between excitable and non-excitable myotubes, we stimulated the myotubes directly with KCl in the myotube compartment after MN stimulation (Figure S4B). Excitable myotubes were considered responsive to KCl through Ca^{2+} wave formation. Approximately 68% of myotubes of total directly KCl-stimulated active myotubes were responsive through MN stimulation (Figure 4D). Quantification of peak values of the Ca^{2+} influx was performed on myotubes demonstrating MN-dependent activity (Figure 4E). To confirm that the Ca^{2+} transients were due to NMJ transmission, NMJs were blocked using the nicotinic AChR competitive antagonist, tubocurarine (DTC) (Afshar Bakooshli et al., 2019), which successfully inhibited the Ca^{2+} transients in our system (Figures 4C and 4E). To assess whether the myotube excitability was

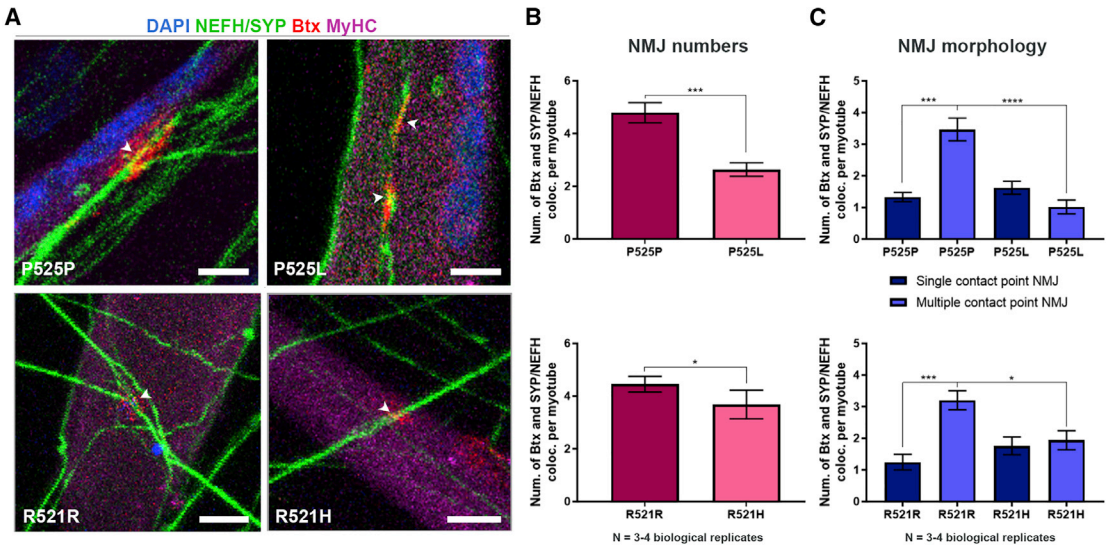

Figure 5. NMJs are impaired in ALS

(A) Confocal micrographs of NMJs with A/L from ALS-*FUS* (P525L, R521H) and isogenic control (P525P, R521R) MN/myotube co-cultures on day 28. Scale bars, 10 μm. Arrowheads: Btx-SYP/NEFH co-localizations.

(B) Quantification of NMJs as Btx and SYP/NEFH co-localizations and expressed per myotube.

(C) Quantification of NMJ single and multiple contact point morphology. Mean ± SEM of three to four biological replicates. (B) Unpaired t test or Mann-Whitney test. (C) Kruskal-Wallis test with Dunn's multiple comparisons test. *p < 0.05, ***p < 0.001, ****p < 0.0001. See also Figures S4, S5, and S7.

dependent on MN presence, we cultured myotubes in 24-well plates and stimulated them with KCl (Figures S4C and S4D). Myotubes were active regardless of MN presence (Figure S4C), and they likewise emitted a Ca^{2+} response independent of DTC treatment, excluding a direct inhibitory effect of DTC on muscle depolarization (Figure S4D). In conclusion, these results confirm the functional MN innervation of myotubes through NMJ formation.

Mutant *FUS*-ALS causes a reduction in NMJ numbers

To assess the effect of disease-causing ALS mutations in this human *in vitro* NMJ model, we used two iPSC lines with mutations in the FUS RNA binding protein (*FUS*) gene. One from a 17-year-old ALS patient with a *de novo* point mutation (P525L) and another one from a 71-year-old ALS patient with a R521H mutation. These patient lines were systematically compared with their corresponding CRISPR-Cas9 gene-edited isogenic P525P and R521R controls, respectively (Guo et al., 2017; Wang et al., 2018). MN differentiation verification with ICC showed no difference in the differentiation potential between the different lines with an approximate expression of 85%–95% of MN markers (Figures S4E–S4G).

NMJ quantifications revealed a higher number of NMJs per myotube in the P525P isogenic control system than in the P525L (Figures 5A, 5B, and S5), indicating a mutant *FUS*-dependent impairment of NMJs. A small difference was also observed between the R521R and R521H co-cultures. In addition, we observed a higher number of multiple contact point NMJs than single contact point NMJs (Figure 5C) in the isogenic control systems, while this difference was not observed in the mutant systems, suggesting that there is a difference in the maturation state between the ALS and control co-cultures.

MN neurite outgrowth and regrowth is diminished in *FUS*-ALS

When culturing the motor unit systems for NMJ quantifications, we also observed a striking difference in neurite outgrowth between the mutant P525L and its isogenic control P525P (Figures 6A and 6B), which was confirmed with our linear Scholl analysis (Figure 6F). No obvious difference in outgrowth was observed in the other pair (R521H and R521R) (Figures S6A, S6B, and S6E). Next, we investigated whether this difference in neurite outgrowth was dependent on myotube presence (Figures S6F–S6K). Interestingly, we observed fewer neurites crossing in smaller bundles in the devices without myotubes, suggesting that myotubes play a role in the polarization of neurites in addition to the volumetric and chemotactic gradient. A similar decrease in neurite outgrowth in *FUS*-mutant P525L in comparison with isogenic control P525P systems was observed without myotubes present, although the difference was less pronounced. To test whether mutant and

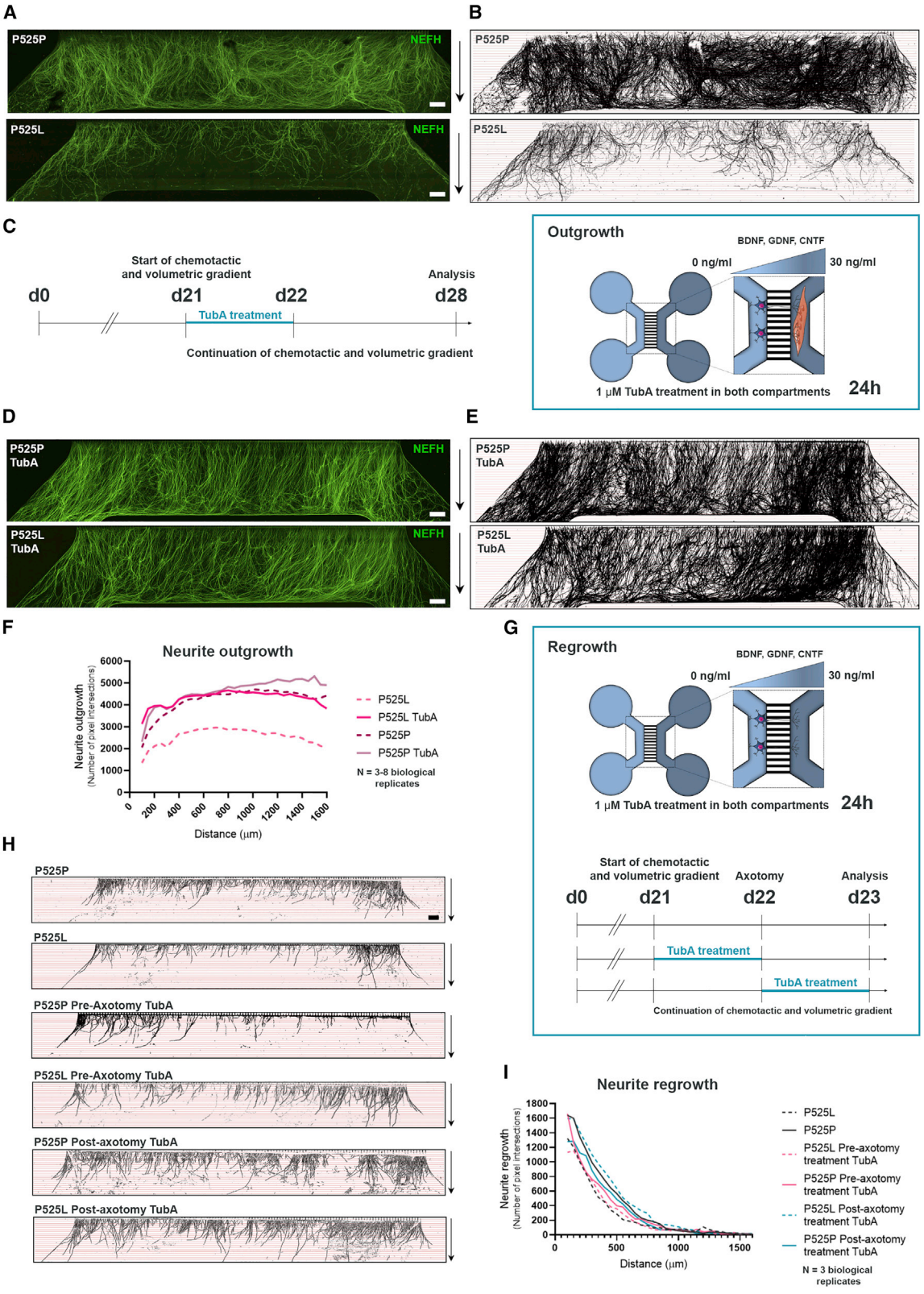

(legend on next page)

isogenic control MNs showed any variation in their initial neurite outgrowth, we cultured MN-NPCs from P525L and control P525P in 24-well plates and analyzed the neurite outgrowth using IncuCyte NeuroTrack software (Figures S7A and S7B). Images were taken every 2 h over the first 24 h after plating of NPCs and no difference in neurite outgrowth was observed between the two lines, suggesting that this phenotype only appears later upon MN maturation.

We next investigated whether a similar difference could be found when evaluating MN neurite regrowth upon axotomy. Therefore, we cultured MNs from *FUS*-mutant P525L and its isogenic control P525P in devices without myotubes, and performed a combined mechanical and chemical axotomy at day 22 of MN maturation (Figure 6G). The neurites were allowed to regrow for 24 h before fixation, imaging, and linear Scholl analysis. Here, we also observed a reduction in the neurite regrowth in the P525L MNs in comparison with the control P525P MNs (Figures 6H and 6I).

Taken together, these results show that the number of NMJs and the MN neurite outgrowth/regrowth are affected by mutations in *FUS* in our motor unit system. These impairments can be successfully rescued by correction of the mutations, emphasizing that the effects are a direct cause of the point mutation in *FUS*.

HDAC6 inhibition rescues mutant *FUS*-mediated impairments of neurite outgrowth and regrowth

Many studies demonstrated beneficial effects of HDAC6 inhibition in various models of neurodegenerative diseases Benoy et al., 2017, 2018; d'Ydewalle et al., 2011; Fazal et al., 2021; Guo et al., 2017; Krukowski et al., 2017; Mao et al., 2017; Van Helleputte et al., 2018). HDAC6 is primarily found in the cytosol where it can deacetylate α-tubulin (Prior et al., 2018; Rossaert and Van Den Bosch, 2020), and we showed previously that HDAC6 inhibition can rescue axonal transport defects in mutant *FUS* MNs (Guo et al., 2017). As the impairment in neurite outgrowth and regrowth could correlate with axonal transport deficits, we investigated whether HDAC6 inhibition could also improve these phenotypes.

Therefore, we first treated our MN-myotube co-cultures with the specific HDAC6 inhibitor, TubA (1 μM), in both the MN and the myotube compartment for 24 h, at day 21 when the chemotactic and volumetric gradient was imposed (Figure 6C). Interestingly, TubA treatment had a striking effect on the neurite outgrowth in the mutant P525L co-cultures, improving the outgrowth of neurites to a similar level as the isogenic control P525P (Figures 6D–6F). TubA treatment also increased the outgrowth of neurites for the other *FUS* mutation (R521H) to a level above the control (Figures S6C and S6E), but had no effect on the initial outgrowth of P525P and P525L MN neurites during the first 24 h of culture (Figures S7A and S7B). TubA treatment had no effect on the previously described cytoplasmic mislocalization of FUS in the P525L MNs (Figures S7C and S7D) (Guo et al., 2017).

We next treated our P525L and P525P MNs in the devices for the regrowth experiment with TubA in both compartments. MNs were treated for 24 h either from days 21 to 22 (pre-axotomy) or from days 22 to 23 (post-axotomy) (Figure 6G). Remarkably, post-axotomy TubA treatment could rescue the *FUS*-mediated impairment in regrowth in the P525L MNs, while pre-axotomy TubA treatment had no effect (Figures 6H and 6I). These results suggest that HDAC6 inhibition could be useful as a treatment after injury rather than a prophylactic therapy.

Figure 6. ALS-dependent impairment in neurite outgrowth and regrowth is rescued by HDAC6 inhibition

(A) Tile scan confocal overviews of neurite outgrowth (NEFH) in the myotube compartment from P525L and P525P cultures at day 28. Arrows (right): growth direction from exit of microgrooves. Scale bars, 300 μm.

(B) Masks of tile scans with intersection lines at every 50 μm starting from microgroove exit.

(C) Schematic representation of outgrowth experimental time course implementing treatment with TubA. At day 21 (d21), both MN and myotube compartments were treated with 1 μM TubA for 24 h in addition to the start of the chemotactic and volumetric gradient.

(D) Tile scan confocal overviews of neurite outgrowth in myotube compartment at day 28 from P525L and P525P MN/myotube co-cultures with TubA treatment. Scale bars, 300 μm.

(E) Masks of tile scans with TubA treatment.

(F) Neurite outgrowth quantifications of the number of pixel intersections in P525L and P525P MN/myotube co-cultures with and without TubA treatment. Mean graph of three to eight biological replicates.

(G) Schematic representation of regrowth experimental time course implementing 24 h treatment with TubA before or after axotomy (day 22).

(H) Masks of tile scan overviews after 24 h neurite regrowth in empty myotube compartment from P525L and P525P cultures without, and with pre-axotomy and post-axotomy treatment with TubA. Arrows (right): growth direction from exit of microgrooves. Scale bar, 300 μm.

(I) Neurite regrowth quantifications of the number of pixel intersections. Mean graph of three biological replicates. Cell illustrations in (C and G) are modified from Smart Servier Medical Art licensed under a Creative Commons Attribution 3.0 Unported License (https://creativecommons.org/licenses/by/3.0/).

See also Figures S4, S6, and S7 and Tables S3 and S4.

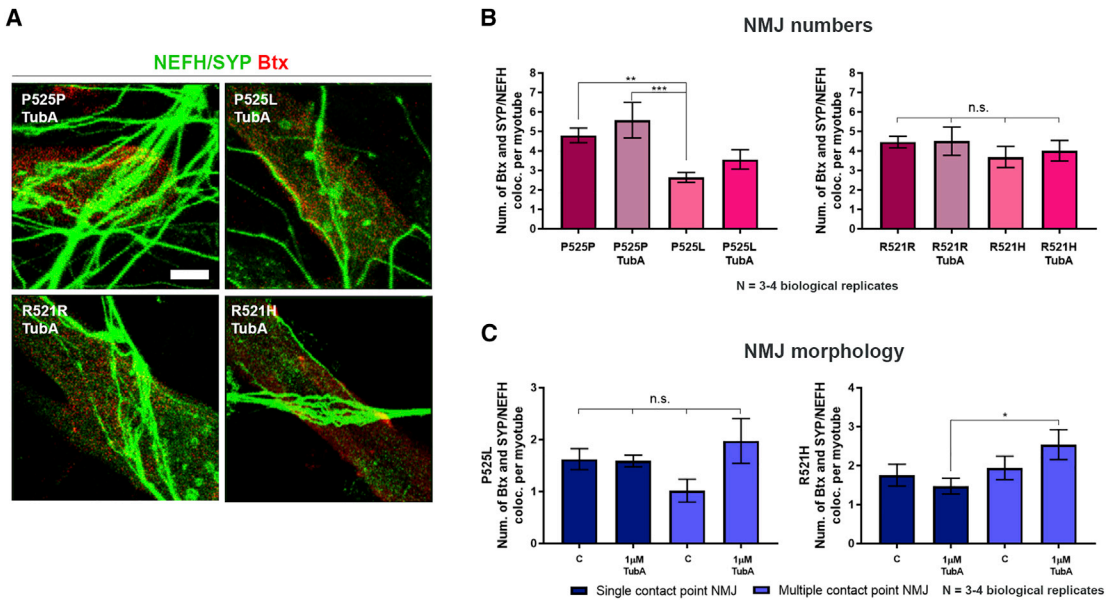

Figure 7. HDAC6 inhibition improves ALS-dependent impairments in NMJ morphology

(A) Confocal micrographs of NMJs with TubA treatment. Scale bar, 10 μm.

(B) Quantification of NMJs as Btx-SYP/NEFH co-localization per myotube with and without TubA treatment. Control data without TubA treatment are identical to Figure 5B.

(C) Morphological analysis of NMJs without (C) and with TubA treatment. Control data (C) are identical to Figure 5C. Mean ± SEM from three to four biological replicates. One-way ANOVA with Tukey's multiple comparisons test or Kruskal-Wallis test with Dunn's multiple comparisons test. *$p < 0.05$, **$p < 0.01$, ***$p < 0.001$.

See also Figures S4 and S7.

HDAC6 inhibition improves NMJ formation in *FUS*-ALS

Since TubA treatment proved to have a beneficial effect on neurite outgrowth and regrowth, and HDAC6 recently has been demonstrated to regulate AChR receptor clustering (Osseni et al., 2020), we next investigated whether this would have an effect on the formation of NMJs. Indeed, compared with our control NMJ data, we observed that 24 h TubA treatment resulted in a tendency toward an increase in total and multiple contact point NMJ numbers in *FUS*-ALS P525L co-culture systems, although this did not reach statistical significance (Figures 7A and 7B). However, we could demonstrate a significant increase in multiple contact point NMJs in the *FUS*-ALS R521H co-cultures reaching similar levels as its corresponding control (R521R, Figure 7C).

In conclusion, we observe a beneficial effect of HDAC6 inhibition on neurite outgrowth, regrowth, and NMJ formation in mutant *FUS* co-cultures illustrating that our *in vitro* system can be used to test new therapeutic strategies for MN diseases.

DISCUSSION

In this study, we developed a standardized co-culture model of hiPSC-derived MN and human primary MAB-derived myotubes in commercial microfluidic devices resulting in the formation of functional human NMJs. We observed that supplementation of A/L promoted polarized MN outgrowth as well as NMJ formation, further enhancing the output of this *in vitro* model. In contrast, mutations in *FUS* had a striking negative effect on neurite outgrowth, neurite regrowth, and NMJ numbers. We could successfully normalize these phenotypes by correcting the point mutations, emphasizing that the impairments are a direct cause of the mutations in *FUS*. Finally, we discovered that HDAC6 inhibition can improve the neurite outgrowth/regrowth impairments and partially restore the formation of NMJs, further prompting HDAC6 inhibition as a potential therapeutic strategy in ALS.

A human NMJ model eliminates the challenge of interspecies variability and reduces the need for overexpression of mutated genes in animal models, which might not fully recapitulate human disease etiology or pathology (Greek and Hansen, 2013; Morrice et al., 2018). In terms of NMJ morphology, it is evident that rodent NMJs are larger, more complex, and less fragmented than human NMJs, and that human NMJs are more stable across the human adult lifespan (Jones et al., 2017). These differences highlight the importance of a human model of NMJs for mechanistic insights in human NMJ physiology and disease.

This model generates single contact point NMJs, which resemble "nummular" morphology in human NMJs from amputates (Jones et al., 2017). In addition, large, irregular multiple contact point NMJs are generated, which present a more complex morphology compared with the nummular NMJs and might therefore be a sign of further maturation.

An advantage of our system is the use of hiPSC-derived MNs, which allows for full adaptability to other MN disorders, including sporadic forms of ALS. In addition, the use of MABs in an NMJ co-culture model has, to our knowledge, not been reported before. MABs present a valid alternative to human satellite cells or myoblasts, since they age less, can undergo more passages, and are generally easier to keep in culture (Dellavalle et al., 2007). Prolonging myotube viability *in vitro* and hence increased NMJ maturity could likely be accomplished by the incorporation of a dynamic adherence system allowing for myotube contractility (Osaki et al., 2018b). However, this requires a redesign of the commercial microfluidic device. An ideal model would contain both iPSC-derived MNs and myotubes from the same donor; however, current protocols display large variabilities in myotube fusion index (Jiwlawat et al., 2018), which lowers the compatibility and compromises the output of our system.

Using our model, we investigated the effects of mutant *FUS* on the formation of human NMJs. Mutations in *FUS* cause the mislocalization of FUS from the nucleus to the cytoplasm, which has recently been reported in other familial as well as sporadic cases of ALS (Tyzack et al., 2019). Interestingly, we saw a reduction in total NMJs with an almost 50% decrease in the *FUS*-P525L system in comparison with the control P525P. The *FUS* mutations did not affect the amount of single contact point NMJs, but had a large impact on the number of multiple contact point NMJs. This is in line with the dying-back mechanism where mature NMJs are lost in disease, while newly formed immature NMJs are made simultaneously to compensate for the lack of muscle innervation. However, we did not observe a significant increase in single contact point NMJs in the mutated system, which could explain such a compensatory mechanism, although a tendency could be observed. As a consequence, we cannot exclude that the P525L findings are a result of a delayed maturation of the system influenced by the impairment in neurite outgrowth. Importantly, as we do not report a clear neurite outgrowth deficiency in the R521H motor unit, this indicates that NMJ numbers are affected independently of maturation of the system but are rather due to the ALS-causing mutation itself. The smaller difference in NMJ numbers between *FUS*-ALS R521H and control R521R correlates with a general observation of mild phenotypes in this late-onset R521H patient in comparison with the rather aggressive phenotypes found in the juvenile-onset P525L-ALS patient in this system.

More and more studies show impaired neurite outgrowth in ALS. These include differences in axonal branching (Akiyama et al., 2019), impairments in neurite elongation speed (Osaki et al., 2018b), and in neurite length (Fujimori et al., 2018). However, the underlying mechanism has yet to be established. We observed that the mutant *FUS*-dependent reduction in neurite outgrowth and regrowth could be rescued by selective inhibition of HDAC6, which suggests a link to the widespread defects of the MN axonal transport machinery (Guo et al., 2019). Our studies in peripheral neuropathies demonstrated a correlation between an improvement of axonal transport due to HDAC6 inhibition and the reinnervation of NMJs *in vivo* (Benoy et al., 2018, 2017; d'Ydewalle et al., 2011; Van Helleputte et al., 2018). Further studies are crucial to investigate the potential of HDAC6 inhibition in ALS, although our *in vivo* results in a *FUS* mouse model already indicate that also other HDACs might play an important role (Rossaert et al., 2019).

Overall, we established a versatile and relatively easy to use motor unit system to study the functionality of human NMJs in culture. This co-culture model has broad application potential and is suited to test therapeutic strategies focusing on reinnervation and/or the stabilization of NMJs.

EXPERIMENTAL PROCEDURES

See supplemental information for detailed descriptions of the methods.

Cell lines and reagents

Healthy human control iPSCs (SBAD2 line) generated from a 51-year-old white male donor were provided by the Stem Cell Institute Leuven (SCIL, Leuven, Belgium), and, in addition, two previously characterized *FUS*-mutant iPSC lines from a 17-year-old male ALS patient carrying a *de novo* mutation (P525L) and a 71-year-old female ALS patient (R521H). The *FUS*-ALS lines were systematically compared with their corresponding CRISPR-Cas9 gene-edited isogenic control (P525P and R521R) generated by CellSystems (Troisdorf, Germany) (Guo et al., 2017; Vandoorne et al., 2019; Wang et al., 2018). Human control primary MABs were obtained from a healthy 58-year-old donor (SCIL).

Chemicals and cell culture reagents were purchased from Thermo Fisher Scientific (Waltham, MA, USA) unless specified otherwise.

Co-culturing myotubes and MNs in a microfluidic device

Human MABs were isolated and cultured as described previously (Dellavalle et al., 2007; Tonlorenzi et al., 2007). The iPSC-derived MN differentiation protocol utilized is based on a modified version of the Maury et al. protocol (Maury et al., 2015) and has previously been described (Guo et al., 2017; Wang et al., 2018).

Day 10 MN-NPCs were seeded in two wells and a channel on one side of the microfluidic device at 125,000 cells per well (total of 250,000 NPCs/device). One week later, MABs were seeded in the two wells and channel opposite to the MNs in the microfluidic device at 100,000 cells per well (total of 200,000 MABs/device). At day 21, a chemotactic and volumetric gradient was established. MN compartments received 100 μL/well neuronal medium without neurotrophic factor, while myotube compartments received 200 μL/well neuronal medium supplemented with 30 ng/mL BDNF (PeproTech, Rocky Hill, NJ, USA, cat. no. 450-02B), GDNF (PeproTech, cat. no. 450-10B) and CNTF (PeproTech, cat. no. 450-13B) in addition to 20 μg/mL laminin (Sigma, cat. no. L2020-1MG) and 0.01 μg/mL recombinant human agrin protein (R&D Systems, cat. no. 6624-AG-050) (A/L). The growth factor and volume gradients, including A/L, were kept at each medium change, which was performed every other day for a week.

TubA treatment

Treatments were made for 24 h with 1–3 μM TubA (Selleckchem, Houston, TX, USA, cat. no. S8049).

Immunocytochemistry and SEM

Immunocytochemistry and SEM are described in the supplemental information. See also Tables S1 and S2.

Neurite axotomy and regrowth

The axotomy was performed using a similar method as described previously (Nijssen et al., 2018).

Neurite outgrowth and regrowth quantifications

Tile scan images of NEFH fluorescence were taken using an inverted Leica SP8 DMI8 confocal microscope and neurites were isolated using ilastik 1.3.3post1 Pixel Classification software. Total number of pixel intersections was quantified per intersection line utilizing a custom ImageJ 1.52p software linear School analysis script.

For MN-NPC neurite outgrowth quantifications, NPCs were imaged for 24 h using an IncuCyte ZOOM device with the IncuCyte ZOOM 2016A software (Essen BioScience) and analyzed with the IncuCyte NeuroTrack Phase Neurites software.

Calcium fluorescent imaging

On day 28 of MN differentiation, myotube compartments were incubated for 25 min with 5 μM Fluo-4 AM (cat. no. F14201). MNs were stimulated with 50 mM KCl and Fluo-4 fluorescence was recorded in the myotube compartment. In addition, myotube compartments were treated with 19 μM of the AChR competitive antagonist tubocurarine hydrochloride pentahydrate (DTC) (Sigma, cat. no. T2379-100G) for 10 min. Myotubes were cultured without MNs in μ-plates (ibidi, Planegg, Germany, cat. no. 82,406) and tested for Ca^{2+} functionality, as well as in devices without MNs to confirm fluidic isolation upon KCl stimulation in the MN compartment. All recordings were acquired and analyzed using a Nikon A1R confocal microscope and NIS-Elements AR 4.30.02 software.

Statistics

Data are presented as mean ± SEM, unless indicated otherwise. Statistical analyses were made in GraphPad Prism 7.04. Data were tested for normal Gaussian distribution using the Anderson-Darling test, D'Agostino-Pearson omnibus normality test, and Shapiro-Wilk normality test. Statistical analyses were determined using unpaired t test or Mann-Whitney test for differences of mean between two groups and one-way ANOVA with Tukey's multiple comparisons test and Kruskal-Wallis test with Dunn's multiple comparisons test for difference of means between multiple groups. *$p < 0.05$, **$p < 0.01$, ***$p < 0.001$, ****$p < 0.0001$.

Data and code availability

The datasets used and analyzed during this study are available in the source data file. ImageJ and Nikon software scripts are available upon request.

SUPPLEMENTAL INFORMATION

Supplemental information can be found online at https://doi.org/10.1016/j.stemcr.2021.03.029.

AUTHOR CONTRIBUTIONS

K.S.D., L.F., and T.V. planned and designed the experiments. E.N.K. and K.S.D. optimized the system. K.S.D. performed most of the experiments and did the data analysis. L.F. and K.S.D. performed ICC. K.S.D. and P.B. performed SEM. A.K. assisted in neurite outgrowth/regrowth quantifications and wrote the Nikon script. B.P. wrote the ImageJ script. E.R. and J.B. helped with the axotomy experiments. M.S. provided mesoangioblasts and valuable ideas for the project. G.G. provided advice for mesoangioblast culturing and differentiation. P.V.D. provided ideas for the project. L.V.D.B. planned and supervised the project. K.S.D. wrote the paper. L.F., T.V., and L.V.D.B. edited the manuscript. All authors read and approved the final version of the paper.

DECLARATION OF INTERESTS

L.V.D.B. has a patent on the use of HDAC inhibitors in Charcot-Marie-Tooth disease (US-2013227717-A1), is scientific co-founder of Augustine Therapeutics and a member of its scientific advisory board. The other authors declare no competing interests.

ACKNOWLEDGMENTS

The authors thank Sebastian Munck and Nikky Corthout from LiMoNe, Research Group Molecular Neurobiology (VIB-KU Leuven) for discussions concerning Ca^{2+} live-cell imaging. This research was supported by the Fulbright Commission to Belgium and Luxembourg, the VIB, the KU Leuven (C1 and "Opening the Future" Fund), the "Fund for Scientific Research Flanders" (FWO-Vlaanderen), the Agency for Innovation by Science and Technology (IWT; SBO-iPSCAF), the Belgian Government (Interuniversity Attraction Poles Program P7/16 initiated by the Belgian Federal Science Policy Office), the Thierry Latran Foundation, the "Association Belge contre les Maladies neuro-Musculaires" (ABMM), Target ALS, and the ALS Liga België (A Cure for ALS). T.V., E.R., and J.B. are

supported by strategic basic research PhD fellowships awarded by FWO-Vlaanderen.

Received: October 22, 2020
Revised: March 23, 2021
Accepted: March 25, 2021
Published: April 22, 2021

REFERENCES

Afshar Bakooshli, M., Lippmann, E.S., Mulcahy, B., Iyer, N., Nguyen, C.T., Tung, K., Stewart, B.A., van den Dorpel, H., Fuehrmann, T., Shoichet, M., et al. (2019). A 3D culture model of innervated human skeletal muscle enables studies of the adult neuromuscular junction. eLife *8*, e44530.

Akiyama, T., Suzuki, N., Ishikawa, M., Fujimori, K., Sone, T., Kawada, J., Funayama, R., Fujishima, F., Mitsuzawa, S., Ikeda, K., et al. (2019). Aberrant axon branching via Fos-B dysregulation in FUS-ALS motor neurons. EBioMedicine *45*, 362–378.

Bellmann, J., Goswami, R.Y., Girardo, S., Rein, N., Hosseinzadeh, Z., Hicks, M.R., Busskamp, V., Pyle, A.D., Werner, C., and Sterneckert, J. (2019). A customizable microfluidic platform for medium-throughput modeling of neuromuscular circuits. Biomaterials *225*, 119537.

Benoy, V., Van Helleputte, L., Prior, R., d'Ydewalle, C., Haeck, W., Geens, N., Scheveneels, W., Schevenels, B., Cader, M.Z., Talbot, K., et al. (2018). HDAC6 is a therapeutic target in mutant GARS-induced Charcot-Marie-Tooth disease. Brain *141*, 673–687.

Benoy, V., Vanden Berghe, P., Jarpe, M., Van Damme, P., Robberecht, W., and Van Den Bosch, L. (2017). Development of improved HDAC6 inhibitors as pharmacological therapy for axonal Charcot-Marie-Tooth disease. Neurotherapeutics *14*, 417–428.

Burden, S.J., Huijbers, M.G., and Remedio, L. (2018). Fundamental molecules and mechanisms for forming and maintaining neuromuscular synapses. Int. J. Mol. Sci. *19*, 490.

Burkin, D.J., Kim, J.E., Gu, M., and Kaufman, S.J. (2000). Laminin and alpha 7 beta 1 integrin regulate agrin-induced clustering of acetylcholine receptors. J. Cell Sci. *113*, 2877–2886.

Campenot, R.B. (1977). Local control of neurite development by nerve growth factor. Proc. Natl. Acad. Sci. U S A *74*, 4516–4519.

d'Ydewalle, C., Krishnan, J., Chiheb, D.M., Van Damme, P., Irobi, J., Kozikowski, A.P., Vanden Berghe, P., Timmerman, V., Robberecht, W., and Van Den Bosch, L. (2011). HDAC6 inhibitors reverse axonal loss in a mouse model of mutant HSPB1-induced Charcot-Marie-Tooth disease. Nat. Med. *17*, 968–974.

Dadon-Nachum, M., Melamed, E., and Offen, D. (2010). The "dying-back" phenomenon of motor neurons in ALS. J. Mol. Neurosci. *43*, 470–477.

de Jongh, R., Spijkers, X.M., Pasteuning-Vuhman, S., Vulto, P., and Pasterkamp, R.J. (2021). Neuromuscular junction-on-a-chip: ALS disease modeling and read-out development in microfluidic devices. J. Neurochem. https://doi.org/10.1111/jnc.15289.

Dellavalle, A., Sampaolesi, M., Tonlorenzi, R., Tagliafico, E., Sacchetti, B., Perani, L., Innocenzi, A., Galvez, B.G., Messina, G., Morosetti, R., et al. (2007). Pericytes of human skeletal muscle are myogenic precursors distinct from satellite cells. Nat. Cell Biol. *9*, 255–267.

Demestre, M., Orth, M., Föhr, K.J., Achberger, K., Ludolph, A.C., Liebau, S., and Boeckers, T.M. (2015). Formation and characterisation of neuromuscular junctions between hiPSC derived motoneurons and myotubes. Stem Cell Res. *15*, 328–336.

Fazal, R., Boeynaems, S., Swijsen, A., De Decker, M., Fumagalli, L., Moisse, M., Vanneste, J., Guo, W., Boon, R., Vercruysse, T., et al. (2021). HDAC6 inhibition restores TDP-43 pathology and axonal transport defects in human motor neurons with TARDBP mutations. EMBO J. *40*, e106177.

Fischer, L.R., Culver, D.G., Tennant, P., Davis, A.A., Wang, M., Castellano-Sanchez, A., Khan, J., Polak, M.A., and Glass, J.D. (2004). Amyotrophic lateral sclerosis is a distal axonopathy: evidence in mice and man. Exp. Neurol. *185*, 232–240.

Fujimori, K., Ishikawa, M., Otomo, A., Atsuta, N., Nakamura, R., Akiyama, T., Hadano, S., Aoki, M., Saya, H., Sobue, G., et al. (2018). Modeling sporadic ALS in iPSC-derived motor neurons identifies a potential therapeutic agent. Nat. Med. *24*, 1579–1589.

Greek, R., and Hansen, L.A. (2013). Questions regarding the predictive value of one evolved complex adaptive system for a second: exemplified by the *SOD1* mouse. Prog. Biophys. Mol. Biol. *113*, 231–253.

Guo, W., Naujock, M., Fumagalli, L., Vandoorne, T., Baatsen, P., Boon, R., Ordovás, L., Patel, A., Welters, M., Vanwelden, T., et al. (2017). HDAC6 inhibition reverses axonal transport defects in motor neurons derived from FUS-ALS patients. Nat. Commun. *8*, 861.

Guo, W., Stoklund Dittlau, K., and Van Den Bosch, L. (2019). Axonal transport defects and neurodegeneration: molecular mechanisms and therapeutic implications. Semin. Cell Dev. Biol. *99*, 133–150.

Guo, X., Gonzalez, M., Stancescu, M., Vandenburgh, H.H., and Hickman, J.J. (2011). Neuromuscular junction formation between human stem cell-derived motoneurons and human skeletal muscle in a defined system. Biomaterials *32*, 9602–9611.

Jiwlawat, N., Lynch, E., Jeffrey, J., Van Dyke, J.M., and Suzuki, M. (2018). Current progress and challenges for skeletal muscle differentiation from human pluripotent stem cells using transgene-free approaches. Stem Cells Int. *11*, 6241681.

Jocher, G., Mannschatz, S.H., Offterdinger, M., and Schweigreiter, R. (2018). Microfluidics of small-population neurons allows for a precise quantification of the peripheral axonal growth state. Front. Cell. Neurosci. *12*, 166.

Jones, R.A., Harrison, C., Eaton, S.L., Llavero Hurtado, M., Graham, L.C., Alkhammash, L., Oladiran, O.A., Gale, A., Lamont, D.J., Simpson, H., et al. (2017). Cellular and molecular anatomy of the human neuromuscular junction. Cell Rep. *21*, 2348–2356.

Krukowski, K., Ma, J., Golonzhka, O., Laumet, G.O., Gutti, T., Van Duzer, J.H., Mazitschek, R., Jarpe, M.B., Heijnen, C.J., and Kavelaars, A. (2017). HDAC6 inhibition effectively reverses chemotherapy-induced peripheral neuropathy. Pain *158*, 1126–1137.

Kummer, T.T., Misgeld, T., Lichtman, J.W., and Sanes, J.R. (2004). Nerve-independent formation of a topologically complex postsynaptic apparatus. J. Cell Biol. *164*, 1077–1087.

Lin, C.Y., Yoshida, M., Li, L.T., Ikenaka, A., Oshima, S., Nakagawa, K., Sakurai, H., Matsui, E., Nakahata, T., and Saito, M.K. (2019). iPSC-derived functional human neuromuscular junctions model the pathophysiology of neuromuscular diseases. JCI Insight *4*, e124299.

Mao, C.X., Wen, X., Jin, S., and Zhang, Y.Q. (2017). Increased acetylation of microtubules rescues human tau-induced microtubule defects and neuromuscular junction abnormalities in *Drosophila*. Dis. Model. Mech. *10*, 1245–1252.

Martineau, É., Di Polo, A., Vande Velde, C., and Robitaille, R. (2018). Dynamic neuromuscular remodeling precedes motor-unit loss in a mouse model of ALS. eLife *7*, e41973.

Maury, Y., Côme, J., Piskorowski, R.A., Salah-Mohellibi, N., Chevaleyre, V., Peschanski, M., Martinat, C., and Nedelec, S. (2015). Combinatorial analysis of developmental cues efficiently converts human pluripotent stem cells into multiple neuronal subtypes. Nat. Biotechnol. *33*, 89–96.

Millet, L.J., and Gillette, M.U. (2012). New perspectives on neuronal development via microfluidic environments. Trends Neurosci. *35*, 752–761.

Mills, R., Taylor-Weiner, H., Correia, J.C., Agudelo, L.Z., Allodi, I., Kolonelou, C., Martinez-Redondo, V., Ferreira, D.M.S., Nichterwitz, S., Comley, L.H., et al. (2018). Neurturin is a PGC-1α1-controlled myokine that promotes motor neuron recruitment and neuromuscular junction formation. Mol. Metab. *7*, 12–22.

Morrice, J.R., Gregory-Evans, C.Y., and Shaw, C.A. (2018). Animal models of amyotrophic lateral sclerosis: a comparison of model validity. Neural Regen. Res. *13*, 2050–2054.

Murray, L.M., Talbot, K., and Gillingwater, T.H. (2010). Neuromuscular synaptic vulnerability in motor neuron disease: amyotrophic lateral sclerosis and spinal muscular atrophy. Neuropathol. Appl. Neurobiol. *36*, 133–156.

Nair, G., Carew, J.D., Usher, S., Lu, D., Hu, X.P., and Benatar, M. (2010). Diffusion tensor imaging reveals regional differences in the cervical spinal cord in amyotrophic lateral sclerosis. Neuroimage *53*, 576–583.

Naumann, M., Pal, A., Goswami, A., Lojewski, X., Japtok, J., Vehlow, A., Naujock, M., Günther, R., Jin, M., Stanslowsky, N., et al. (2018). Impaired DNA damage response signaling by *FUS*-NLS mutations leads to neurodegeneration and FUS aggregate formation. Nat. Commun. *9*, 335.

Nijssen, J., Aguila, J., Hoogstraaten, R., Kee, N., and Hedlund, E. (2018). Axon-seq decodes the motor axon transcriptome and its modulation in response to ALS. Stem Cell Reports *11*, 1565–1578.

Osaki, T., Sivathanu, V., and Kamm, R.D. (2018a). Engineered 3D vascular and neuronal networks in a microfluidic platform. Sci. Rep. *8*, 5168.

Osaki, T., Uzel, S.G.M., and Kamm, R.D. (2018b). Microphysiological 3D model of amyotrophic lateral sclerosis (ALS) from human iPS-derived muscle cells and optogenetic motor neurons. Sci. Adv. *4*, eaat5847.

Osseni, A., Ravel-chapuis, A., Thomas, J., Gache, V., Schaeffer, L., and Jasmin, B.J. (2020). HDAC6 regulates microtubule stability and clustering of AChRs at neuromuscular junctions. JCB *219*, e201901099.

Plomp, J.J. (2018). Neuromuscular junction physiology and pathophysiology. In *Myasthenia Gravis and Related Disorders*, H.J. Kaminski and L.L. Kusner, eds. (Springer International Publishing), pp. 1–12.

Prior, R., Van Helleputte, L., Klingl, Y.E., and Van Den Bosch, L. (2018). HDAC6 as a potential therapeutic Target for peripheral nerve disorders. Expert Opin. Ther. Targets *22*, 993–1007.

Puttonen, K.A., Ruponen, M., Naumenko, N., Hovatta, O.H., Tavi, P., and Koistinaho, J. (2015). Generation of functional neuromuscular junctions from human pluripotent stem cell lines. Front. Cell. Neurosci. *9*, 473.

Robberecht, W., and Philips, T. (2013). The changing scene of amyotrophic lateral sclerosis. Nat. Rev. Neurosci. *14*, 248–264.

Rossaert, E., and Van Den Bosch, L. (2020). HDAC6 inhibitors: translating genetic and molecular insights into a therapy for axonal CMT. Brain Res. *1733*, 146692.

Rossaert, E., Pollari, E., Jaspers, T., Van Helleputte, L., Jarpe, M., Van Damme, P., De Bock, K., Moisse, M., and Van Den Bosch, L. (2019). Restoration of histone acetylation ameliorates disease and metabolic abnormalities in a FUS mouse model. Acta Neuropathol. Commun. *7*, 107.

Rotini, A., Martínez-Sarrà, E., Duelen, R., Costamagna, D., Di Filippo, E.S., Giacomazzi, G., Grosemans, H., Fulle, S., and Sampaolesi, M. (2018). Aging affects the in vivo regenerative potential of human mesoangioblasts. Aging Cell *17*, e12714.

Santhanam, N., Kumanchik, L., Guo, X., Sommerhage, F., Cai, Y., Jackson, M., Martin, C., Saad, G., McAleer, C.W., Wang, Y., et al. (2018). Stem cell derived phenotypic human neuromuscular junction model for dose response evaluation of therapeutics. Biomaterials *166*, 64–78.

So, E., Mitchell, J.C., Memmi, C., Chennell, G., Vizcay-Barrena, G., Allison, L., Shaw, C.E., and Vance, C. (2018). Mitochondrial abnormalities and disruption of the neuromuscular junction precede the clinical phenotype and motor neuron loss in hFUSWT transgenic mice. Hum. Mol. Genet. *27*, 463–474.

Southam, K.A., King, A.E., Blizzard, C.A., McCormack, G.H., and Dickson, T.C. (2013). Microfluidic primary culture model of the lower motor neuron-neuromuscular junction circuit. J. Neurosci. Methods *218*, 164–169.

Tallon, C., Russell, K.A., Sakhalkar, S., Andrapallayal, N., and Farah, M.H. (2016). Length-dependent axo-terminal degeneration at the neuromuscular synapses of type II muscle in *SOD1* mice. Neuroscience *312*, 179–189.

Taylor, A.M., Blurton-Jones, M., Rhee, S.W., Cribbs, D.H., Cotman, C.W., and Jeon, N.L. (2005). A microfluidic culture platform for CNS axonal injury, regeneration and transport. Nat. Methods *2*, 599–605.

Tonlorenzi, R., Dellavalle, A., Schnapp, E., Cossu, G., and Sampaolesi, M. (2007). Isolation and characterization of mesoangioblasts from mouse, dog, and human tissues. Curr. Protoc. Stem Cell Biol. *2*, 2B.1.

Tyzack, G.E., Luisier, R., Taha, D.M., Neeves, J., Modic, M., Mitchell, J.S., Meyer, I., Greensmith, L., Newcombe, J., Ule, J., et al. (2019). Widespread FUS mislocalization is a molecular hallmark of amyotrophic lateral sclerosis. Brain *142*, 2572–2580.

Umbach, J.A., Adams, K.L., Gundersen, C.B., and Novitch, B.G. (2012). Functional neuromuscular junctions formed by embryonic stem cell-derived motor neurons. PLoS One *7*, e36049.

Van Helleputte, L., Kater, M., Cook, D.P., Eykens, C., Rossaert, E., Haeck, W., Jaspers, T., Geens, N., Vanden Berghe, P., Gysemans, C., et al. (2018). Inhibition of histone deacetylase 6 (HDAC6) protects against vincristine-induced peripheral neuropathies and inhibits tumor growth. Neurobiol. Dis. *111*, 59–69.

Vandoorne, T., Veys, K., Guo, W., Sicart, A., Vints, K., Swijsen, A., Moisse, M., Eelen, G., Gounko, N.V., Fumagalli, L., et al. (2019). Differentiation but not ALS mutations in FUS rewires motor neuron metabolism. Nat. Commun. *10*, 4147.

Walker, A.K., Spiller, K.J., Ge, G., Zheng, A., Xu, Y., Zhou, M., Tripathy, K., Kwong, L.K., Trojanowski, J.Q., and Lee, V.M.Y. (2015). Functional recovery in new mouse models of ALS/FTLD after clearance of pathological cytoplasmic TDP-43. Acta Neuropathol. *130*, 643–660.

Wang, H., Guo, W., Mitra, J., Hegde, P.M., Vandoorne, T., Eckelmann, B.J., Mitra, S., Tomkinson, A.E., Van Den Bosch, L., and Hegde, M.L. (2018). Mutant *FUS* causes DNA ligation defects to inhibit oxidative damage repair in amyotrophic lateral sclerosis. Nat. Commun. *9*, 3683.

Zahavi, E.E., Ionescu, A., Gluska, S., Gradus, T., Ben-Yaakov, K., and Perlson, E. (2015). A compartmentalized microfluidic neuromuscular co-culture system reveals spatial aspects of GDNF functions. J. Cell Sci. *128*, 1241–1252.

Zhang, B.G.X., Quigley, A.F., Bourke, J.L., Nowell, C.J., Myers, D.E., Choong, P.F.M., and Kapsa, R.M.I. (2016). Combination of agrin and laminin increase acetylcholine receptor clustering and enhance functional neuromuscular junction formation in vitro. Dev. Neurobiol. *76*, 551–565.

Stem Cell Reports, Volume *16*

Supplemental Information

Human motor units in microfluidic devices are impaired by *FUS* mutations and improved by HDAC6 inhibition

Katarina Stoklund Dittlau, Emily N. Krasnow, Laura Fumagalli, Tijs Vandoorne, Pieter Baatsen, Axelle Kerstens, Giorgia Giacomazzi, Benjamin Pavie, Elisabeth Rossaert, Jimmy Beckers, Maurilio Sampaolesi, Philip Van Damme, and Ludo Van Den Bosch

Supplemental Information

Supplemental table of contents

Figure S1

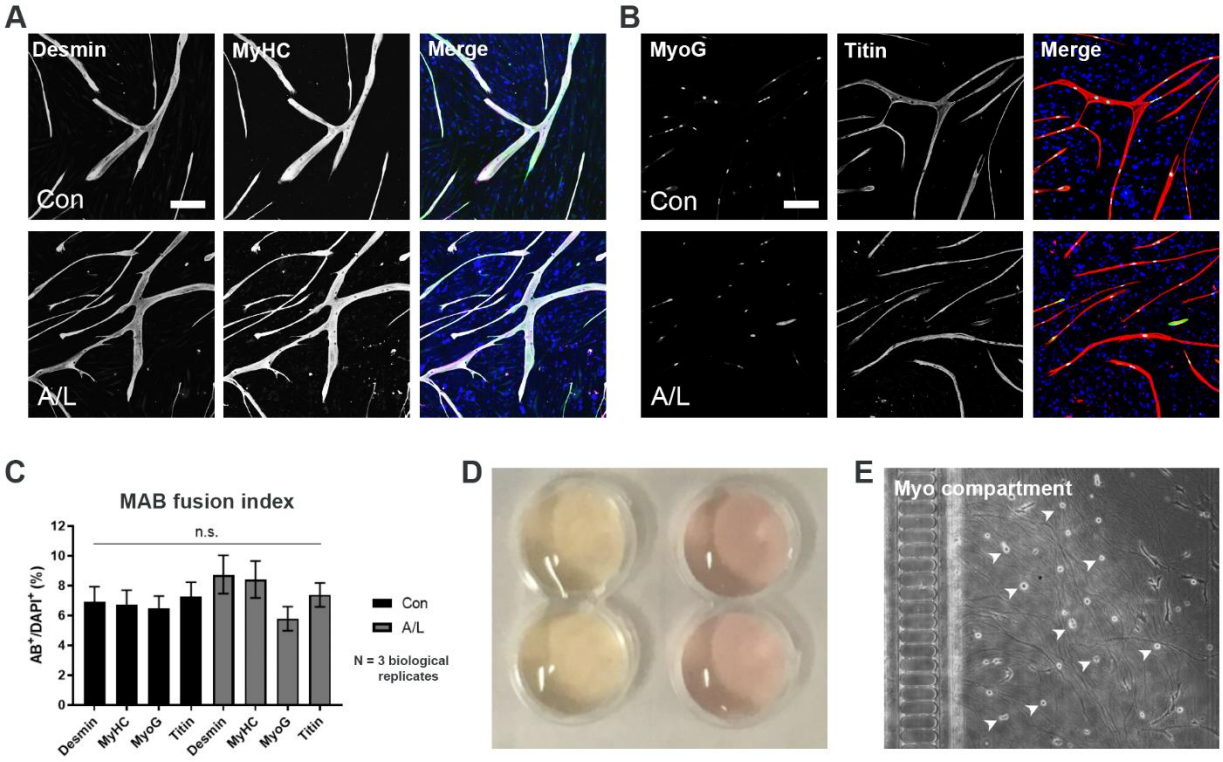

Figure S1: Myotube fusion index, fluidic isolation in microfluidic device and optimization of co-culture protocol. Related to figure 1.

A-B. Representative confocal images of myotube markers (AB^+): desmin, myosin heavy chain (MyHC), myogenin (MyoG) and titin in agrin (0.01 µg/ml) and laminin (20 µg/ml) supplemented conditions (A/L) and untreated controls (Con) after 10 days of differentiation. **C**. Quantification of MAB's fusion into multinucleated myotubes (fusion index). Control data are identical to Figure 1.D. All data represent mean ± s.e.m. of 3 biological replicates and statistical analysis in panel **C** was performed using one-way Anova and Tukey's multiple comparisons test. **D.** Confirmation of fluidic isolation between left and right compartments in an XC150 microfluidic device. By establishing a volumetric gradient, the pH-sensitive medium on the motor neurons changes colour to yellow (left side), whereas the medium in the empty compartment remains pink (right side) after 24 h. **E.** Maturation of MN in a device for 2 weeks (=day 24) before seeding of MABs (arrowheads). In order to prolong MN maturation and the sustainability of the co-culture system, we attempted to plate MABs at day 24 of MN differentiation. However, two weeks of MN maturation in the device resulted in large amounts of spontaneous neurite crossing, which inhibited the attachment of MABs in the channel (arrowheads). Due to the lack of myotube formation, we performed the seeding of MABs at day 17 (Figure 1.E).

Figure S2

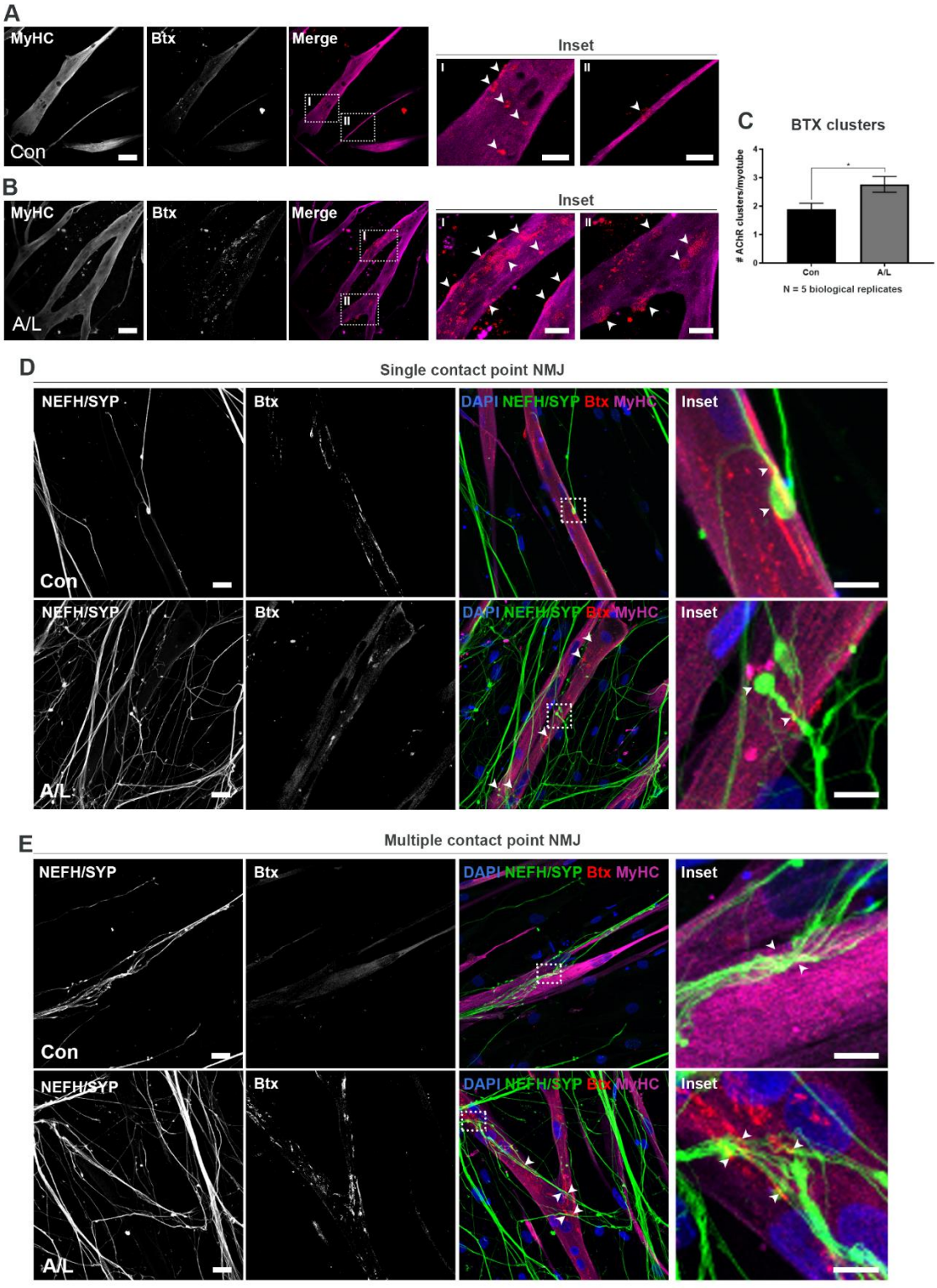

Figure S2: Agrin and laminin treatment enhance acetylcholine receptor clustering and NMJ formation. Related to Figure 3.

A-B. Representative ICC images of MyHC-positive myotubes with Btx-positive AChR clusters after 10 days differentiation in control conditions (Con) and with supplements of agrin and laminin (A/L). Scale bar: 75 µm.

Insets represent a magnification of AChR clusters (arrowheads). Inset scale bar: 25 μm. **C.** Quantifications of AChR cluster number per myotube. The data represent mean ± s.e.m. of 3 biological replicates and statistical analysis was performed using unpaired t-test with *p<0.05. **D-E.** Confocal micrographs of NMJs in agrin and laminin supplemented conditions (A/L) and untreated controls (Con) at 28 days of MN differentiation in XC150 microfluidic devices. NEFH- and SYP-positive motor neuronal axons either form a single contact point connection with myotubes forming rudimental NMJs (**D**) or they fan out upon interaction with myotubes and create multiple contact point NMJs (**E**). Scale bar: 25 μm. Arrowheads mark co-localizations between SYP/NEFH and Btx. Inset scale bar: 10 μm.

Figure S3

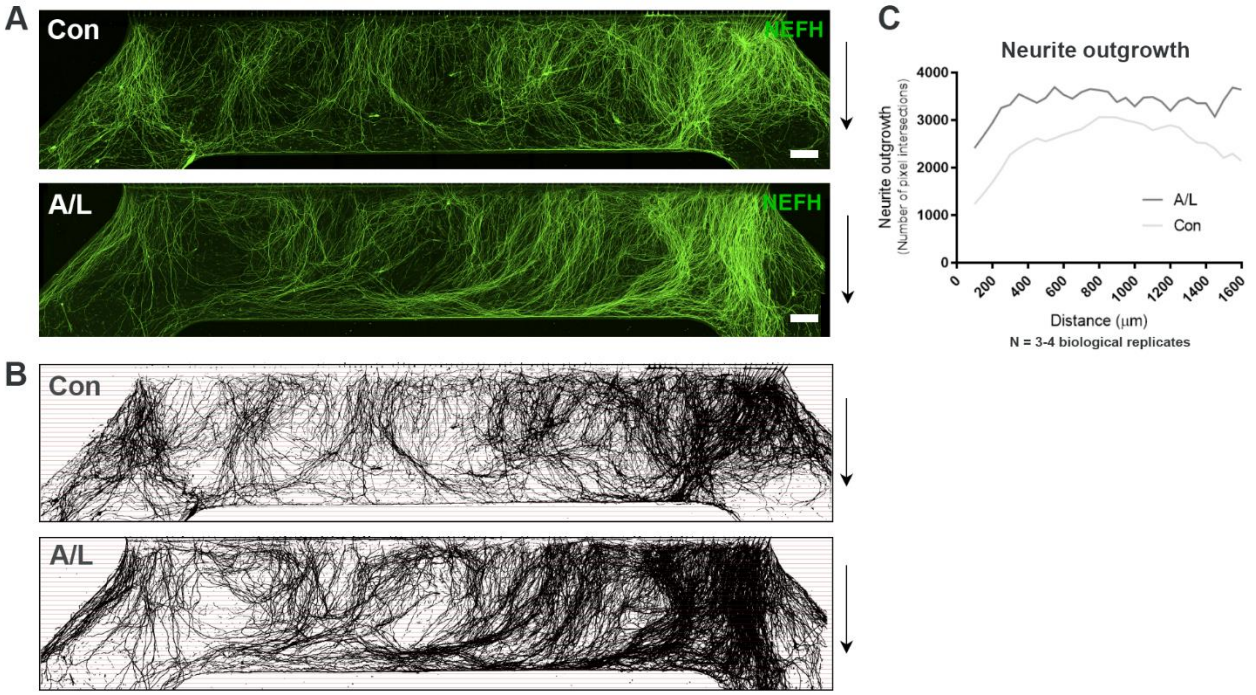

Figure S3: Agrin and laminin improve neurite outgrowth. Related to Figure 3.
A. Tile scan confocal overviews of neurite outgrowth in myotube compartment at day 28 of MN differentiation. Arrows (right) depict growth direction from exit of microgrooves. Scale bar: 300 μm. **B.** Masks of tile scans with intersection lines at every 50 μm from microgroove exit. **C.** Neurite outgrowth quantifications of the number of pixel intersections in each condition (A/L and Con). Panel **C** was performed in 3-4 biological replicates with mean graphs shown.

Figure S4

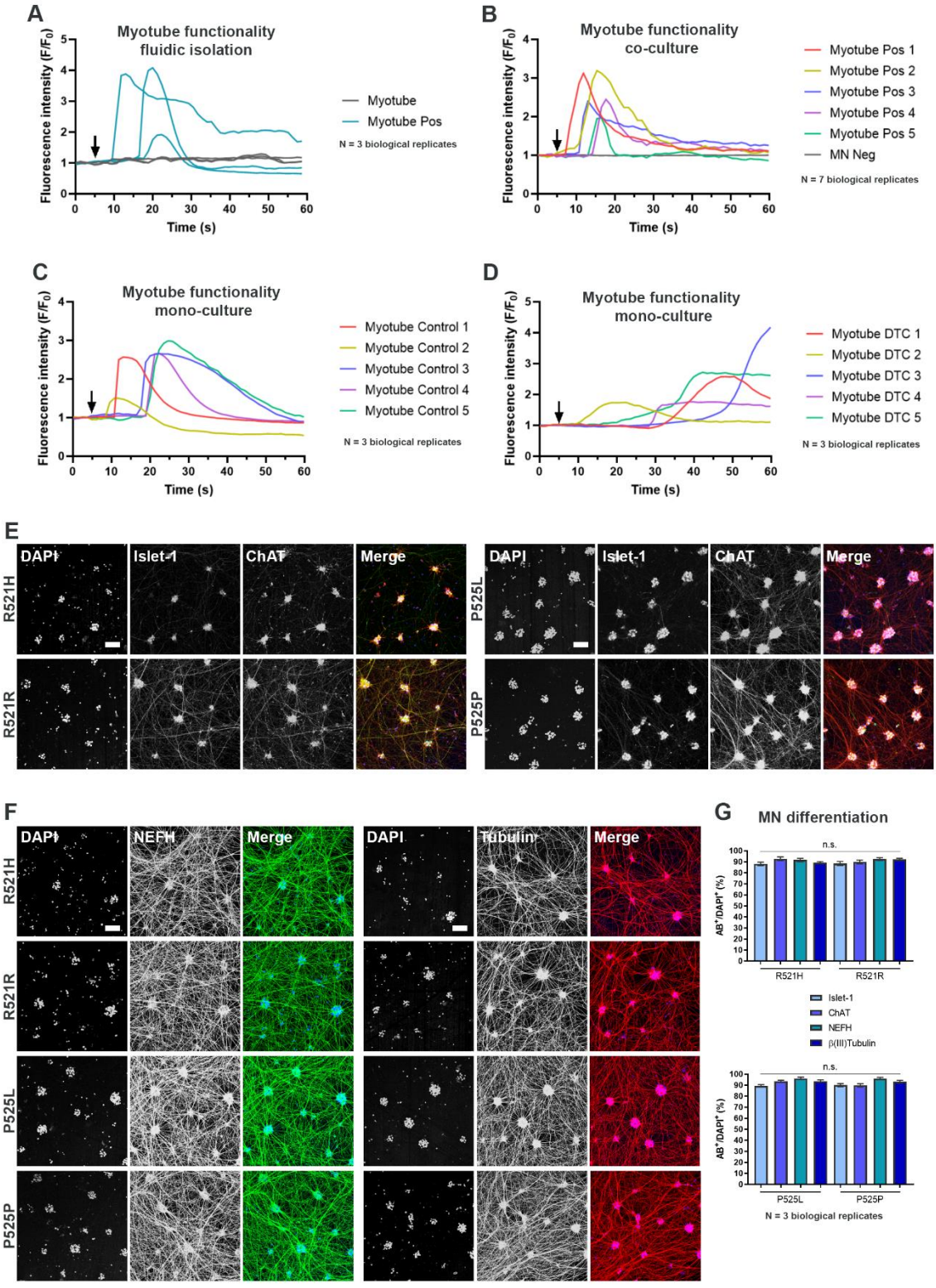

Figure S4. Myotube functionality controls and *FUS*-ALS MN differentiation verification related to Figure 4-7.

A. Representative Ca^{2+} influx curves in myotubes cultured in microfluidic devices without MNs in order to confirm fluidic isolation during KCl stimulation (arrow). The empty MN compartment was first stimulated with

50mM KCl (Myotube), followed by a direct KCl stimulation of myotubes in myotube compartment (Myotube pos). **B.** Representative Ca^{2+} influx curves in myotubes in co-culture with MNs after direct KCl stimulation (arrow) of myotubes in myotube compartment (Myotube Pos 1-5). MN Neg curve represent a recording of the MN compartment after MN stimulation with KCl confirming a fluidic isolation between compartments during incubation with the Fluo-4 dye. **C**. Representative Ca^{2+} influx curves in myotubes cultured without MNs. Arrow mark KCl stimulation. **D**. Representative Ca^{2+} influx curves in myotubes cultured without MNs after 10 min treatment with 19 µM nicotinic AChR competitive antagonist tubocurarine. Arrow mark KCl stimulation. Data in **A** and **B** represents 3 and 7 biological replicates, respectively, while **C** and **D** represent 3 biological replicates with each three technical replicates. **E-F.** Confocal images of mutant *FUS* MNs (P525L, R521H) and isogenic control MNs (P525P, R521R). MNs are stained with MN markers Islet-1 and choline acetyltransferase (ChAT) (**E**) and neurofilament heavy chain (NEFH) as well as the pan-neuronal marker βIII-tubulin (Tubulin) (**F**) at day 28 of MN differentiation. Scale bar: 75 µm. **G.** Relative number of cells positive for MN and pan-neuronal markers. The data in panel **G** represent mean ± s.e.m and statistical analysis was performed using Kruskal-Wallis test with Dunn's multiple comparisons test from 3 biological replicates.

Figure S5

A

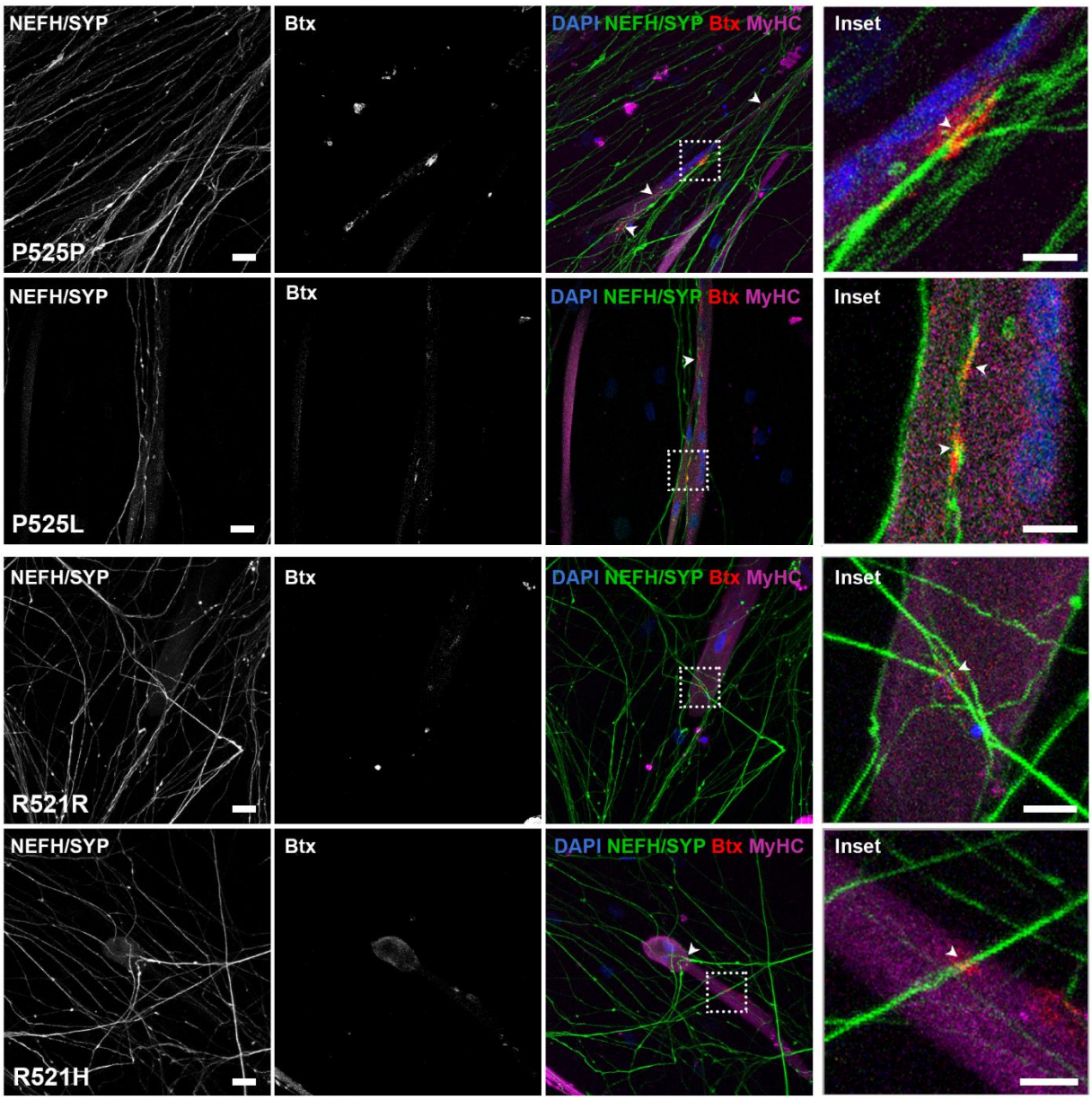

Figure S5: NMJ images related to Figure 5.
A. Confocal micrographs of NMJs in A/L supplemented conditions from *FUS*-mutant MN/myotube co-cultures (P525L, R521H) and isogenic control MN/myotube co-cultures (P525P, R521R) at 28 days of MN differentiation in XC150 microfluidic devices. Scale bar: 25 µm. Arrowheads mark co-localizations between SYP/NEFH and Btx. Inset scale bar: 10 µm.

Figure S6

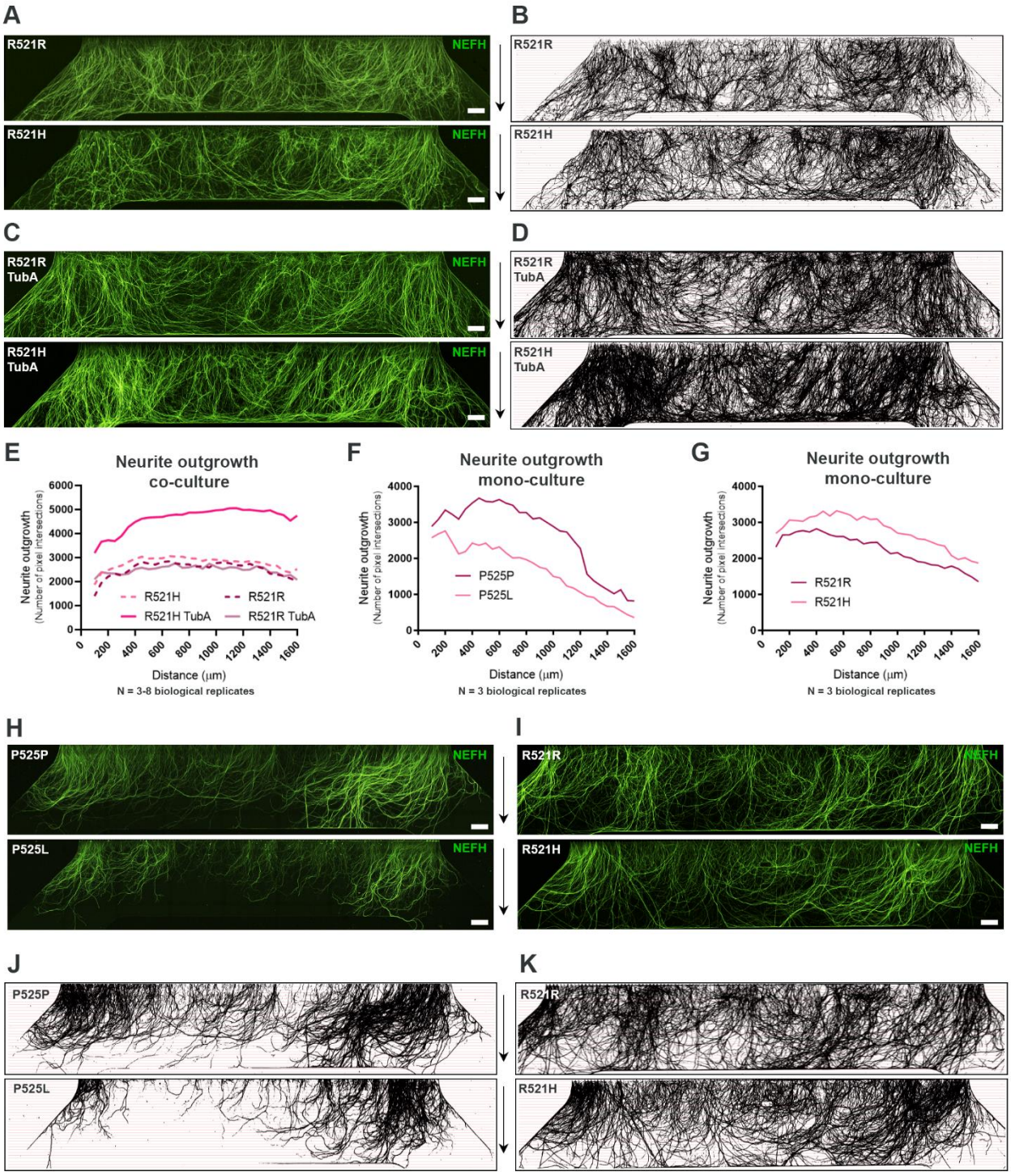

Figure S6: Neurite outgrowth related to Figure 6.
A. Tile scan confocal overviews of neurite outgrowth (NEFH) in myotube compartment from mutant *FUS* (R521H) and isogenic control (R521R) MN/myotubes co-cultures at day 28 of MN differentiation. Arrows (right) depict growth direction from exit of microgrooves. Scale bar: 300 µm. **B**. Masks of tile scans with intersection lines at every 50 µm from microgroove exit. **C**. Tile scan images of neurite outgrowth in R521R and R521H MN/myotube co-cultures after 24 h of Tubastatin A (TubA) treatment. Scale bar: 300 µm. **D**. Masks of tile scans with TubA treatment. **E**. Neurite outgrowth quantifications of pixel intersections in R521R and R521H MN/myotube co-cultures with and without treatment with TubA. **F-G**. Neurite outgrowth quantifications in

myotube compartment from mutant *FUS* (P525L, R521H) and corresponding isogenic controls (P525P, R521R) of the number of pixel intersections in MN cultures without myotubes. **H-J**. Tile scan confocal overviews of neurite outgrowth in MN cultures without myotubes. **J-K**. Masks of tile scans cultured without myotubes with intersection lines at every 50 µm from microgroove exit. Data is from 3-8 biological replicates.

Figure S7

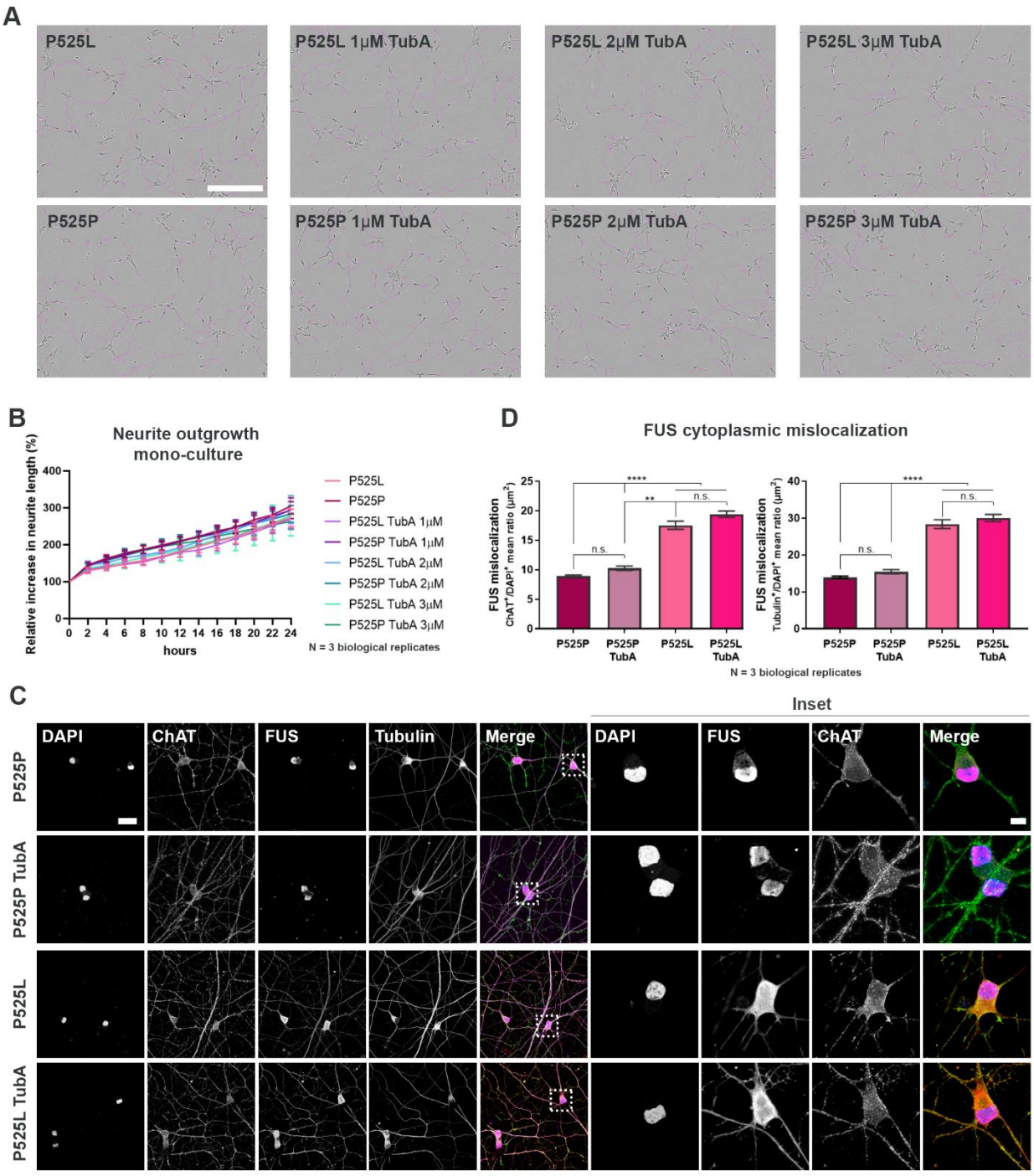

Figure S7. Neurite outgrowth in mono-culture and FUS mislocalization. Related to Figure 5-7.
A. Representative IncuCyte bright field images 24 h after plating of *FUS*-ALS patient line P525L and isogenic control P525P day 10 MN-NPCs with 1-3 µM Tubastatin A (TubA) treatment and controls receiving no treatment. Neurite are marked using IncuCyte Phase Neurite mask. Scale bar: 200 µm. **B**. Quantifications of relative increase in neurite length. Data represent mean ± s.e.m and statistical analysis was performed using one-way Anova with Tukey's multiple comparisons test from 3 biological replicates with two technical replicates in each. **C**. Representative confocal micrographs of day 22 MNs from *FUS*-ALS patient line P525L and isogenic control P525P with and without 24h of 1 µM TubA treatment. Treatment was initiated from day 21 to day 22 of

MN differentiation. Scale bar: 200 µm. Inset: magnification of MN soma. Inset scale bar: 10 µm. **D**. Quantifications of cytoplasmic/nucleus ratio of FUS. Data represent mean ± s.e.m and statistical analysis was performed using one-way Anova with Tukey's multiple comparisons test or Kruskal-Wallis test with Dunn's multiple comparisons test from 3 biological replicates with two technical replicates in each. Outliers (Q=1%) were removed. **p <0.01 and ****p <0.0001.

Table S1: Primary antibody overview. Related to Figure 1-3 and 5-7.

Antibody	Dilution	Company	Antibody Registry* Identifier
Rabbit anti-neurofilament heavy chain (NEFH)	1:1000	Abcam, Cat N° AB8135	AB_306298
Rabbit anti-synaptophysin (SYP)	1:1000	Cell Signaling, Cat N° 5461S	AB_10698743
Mouse anti-myosin heavy chain (MyHC)	1:20	In-house, SCIL	
Goat anti-choline acetyltransferase (ChAT)	1:500	Millipore, Cat N° ab144P	AB_2079751
Rabbit anti-islet 1	1:400	Millipore, Cat N° ab4326	AB_10563961
Mouse anti-βIII-tubulin	1:500	Abcam, Cat N° ab7751	AB_306045
Mouse anti-titin	1:300	Developmental Studies Hybridoma Bank, Cat N° 9 D10	AB_528491
Rabbit anti-myogenin (MyoG)	1:500	Abcam, Cat N° Ab124800	AB_10971849
Rabbit anti-desmin	1:200	Abcam, Cat N° Ab15200	AB_301744
Rabbit anti-FUS/TLS	1:50	Proteintech, Cat N° 115701-AP	AB_2247082

***** https://antibodyregistry.org/

Table S2: Secondary antibody overview. Related to Figure 1-3 and 5-7.

Antibody	Dilution	Company	Antibody Registry* Identifier
Alexa Flour™ IgG (H+L) 488 donkey-anti-rabbit	1:1000	Thermo Fisher Scientific, Cat N° A21206	AB_2535792
Alexa Flour™ IgG (H+L) 555 donkey-anti-goat	1:1000	Thermo Fisher Scientific, Cat N° A21432	AB_2535853
Alexa Flour™ IgG (H+L) 555 donkey-anti-mouse	1:1000	Thermo Fisher Scientific, Cat N° A31570	AB_2536180
Alexa Flour™ IgG (H+L) 647 donkey-anti-mouse	1:1000	Thermo Fisher Scientific, Cat N° A31571	AB_162542
α-bungarotoxin (Btx) Alexa Flour™ 555	1:1000	Thermo Fisher Scientific, Cat N° B35451	AB_2617152

***** https://antibodyregistry.org/

Table S3: Neurite outgrowth thresholds. Related to Figure 6.

Sample ID (MN/Myotube co-cultures)	Threshold (%)	Sample ID (MN/Myotube co-cultures)	Threshold (%)	Sample ID TubA treatment (MN/Myotube co-cultures)	Threshold (%)
A/L biological replicate 1	60	R521H biological replicate 1	35	P525L biological replicate 1	50
A/L biological replicate 2	60	R521H biological replicate 2	70	P525L biological replicate 2	60
A/L biological replicate 3	70	R521H biological replicate 3	70	P525L biological replicate 3	55
A/L biological replicate 4	70	R521H biological replicate 4	30	P525P biological replicate 1	55
Control biological replicate 1	40	R521H biological replicate 5	50	P525P biological replicate 2	50
Control biological replicate 2	45	R521H biological replicate 6	50	P525P biological replicate 3	55
Control biological replicate 3	60	R521H biological replicate 7	50	R521H biological replicate 1	60
P525L biological replicate 1	40	R521H biological replicate 8	50	R521H biological replicate 2	50
P525L biological replicate 2	40	R521R biological replicate 1	50	R521H biological replicate 3	50
P525L biological replicate 3	45	R521R biological replicate 2	60	R521H biological replicate 4	60
P525L biological replicate 4	50	R521R biological replicate 3	50	R521H biological replicate 5	50
P525L biological replicate 5	45	R521R biological replicate 4	45	R521R biological replicate 1	30
P525L biological replicate 6	50	R521R biological replicate 5	35	R521R biological replicate 2	25
P525P biological replicate 1	70	R521R biological replicate 6	50	R521R biological replicate 3	50
P525P biological replicate 2	50	**Sample ID (MN without myotubes)**	**Threshold (%)**	**Sample ID (MN without myotubes)**	**Threshold (%)**
P525P biological replicate 3	60	P525L biological replicate 1	35	R521H biological replicate 1	50
P525P biological replicate 4	60	P525L biological replicate 2	35	R521H biological replicate 2	40
P525P biological replicate 5	50	P525L biological replicate 3	35	R521H biological replicate 3	30
P525P biological replicate 6	35	P525P biological replicate 1	35	R521R biological replicate 1	50
P525P biological replicate 7	55	P525P biological replicate 2	35	R521R biological replicate 2	50
		P525P biological replicate 3	35	R521R biological replicate 3	40

Table S4: Neurite regrowth thresholds. Related to Figure 6.

Sample ID Controls	Threshold (%)	Sample ID Pre-axotomy TubA treatment	Threshold (%)	Sample ID Post-axotomy TubA treatment	Threshold (%)
P525L biological replicate 1, technical replicate 1	25	P525L biological replicate 1, technical replicate 1	40	P525L biological replicate 1, technical replicate 1	50
P525L biological replicate 1, technical replicate 2	45	P525L biological replicate 1, technical replicate 2	20	P525L biological replicate 1, technical replicate 2	20
P525L biological replicate 2, technical replicate 1	15	P525L biological replicate 2, technical replicate 1	25	P525L biological replicate 2, technical replicate 1	15
P525L biological replicate 2, technical replicate 2	20	P525L biological replicate 2, technical replicate 2	25	P525L biological replicate 2, technical replicate 2	20
P525L biological replicate 3, technical replicate 1	15	P525L biological replicate 3, technical replicate 1	20	P525L biological replicate 3, technical replicate 1	20
P525L biological replicate 3, technical replicate 2	15	P525L biological replicate 3, technical replicate 2	20	P525L biological replicate 3, technical replicate 2	20
P525P biological replicate 1, technical replicate 1	35	P525P biological replicate 1, technical replicate 1	40	P525P biological replicate 1, technical replicate 1	50
P525P biological replicate 1, technical replicate 2	20	P525P biological replicate 1, technical replicate 2	50	P525P biological replicate 1, technical replicate 2	40
P525P biological replicate 2, technical replicate 1	20	P525P biological replicate 2, technical replicate 1	15	P525P biological replicate 2, technical replicate 1	20
P525P biological replicate 2, technical replicate 2	20	P525P biological replicate 2, technical replicate 2	15	P525P biological replicate 2, technical replicate 2	20
P525P biological replicate 3, technical replicate 1	15	P525P biological replicate 3, technical replicate 1	20	P525P biological replicate 3, technical replicate 1	20
P525P biological replicate 3, technical replicate 2	15	P525P biological replicate 3, technical replicate 2	20	P525P biological replicate 3, technical replicate 2	15

Supplemental Experimental procedures

Ethics

Healthy human control iPSCs (SBAD2 line) is derived by StemBANCC and was previously provided to SCIL by Dr. P. Jennings (Innsbruck University, Austria) as part of the EU-ToxRisk consortium (1). The CRISPR/Cas9 gene-edited isogenic controls (P525P and R521R) were generated by Cellsystems (Troisdorf, Germany). iPSCs were transfected with gRNA vector, Cas9 vector, and donor DNA, and transfected cells were selected with puromycin for 2 days. Single clones were genotyped with genomic DNA PCR and subsequently sequenced, which confirmed the absence of the FUS mutations (2,3).
Written informed consent was obtained from the subjects who provided their samples for iPSC generation and MAB harvest. MAB isolation and characterisation was approved by the medical ethics committee of the University Hospital Leuven (n° S5732-ML11268). The generation of iPSCs from the healthy control was approved by the UK's main research ethics committee as part of the StemBANCC project, while the use of iPSC in this study was approved by the ethics committee of KU Leuven. The use of *FUS* patient fibroblasts and generation of iPSCs was approved by the ethics committee of the University Hospital Leuven (n° S50354 and S63792). All cells were routinely tested for mycoplasma contamination with MycoAlert Mycoplasma Detection Kit (Lonza, Rockland, ME, USA, Cat N° LT07-318).

Preparation of microfluidic devices

Microfluidic devices (Xona™ Microfluidics, Temecula, CA, USA; Cat N° SND75 (microgroove length: 75 μm) and Cat N° XC150 (microgroove length: 150 μm)) and 7.8mil Aclar 33C sheets (Electron Microscopy Sciences, Hatfield, PA, USA, Cat N° 50425-25) were sterilized in 70% ethanol and left to air-dry in the laminar flow. Devices were placed individually in 10 cm petri dishes for easy handling. SND75 devices and Aclar sheets were coated separately using 100 µg/ml poly L-ornithine (PLO) (Sigma, St. Louis, MO USA, Cat N° P3655-100MG) in DPBS (Cat N° 14190250) prior to mounting of devices on the Aclar sheet. XC150 devices were coated directly using 100 µg/mL PLO in DPBS. Importantly, avoidance of air bubble formation was ensured during the coating of the channels by never removing liquid directly from channels.
All coated material was incubated at 37°C, 5% CO_2 for 3 h and subsequently washed twice in DPBS and once in sterile water. SND75 devices and Aclar sheets were left in the laminar flow cabinet for complete drying (20-30 min) before mounting of devices onto Aclar sheets. Assembly was performed in the laminar flow under a microscope with the use of a forceps to ensure the complete alignment of channels, grooves and borders of the wells. Once assembled, devices were checked for leakage and coated with 20 µg/ml laminin (Sigma, Cat N° L2020-1MG) in Neurobasal medium (Cat N° 21103049). A volume difference was established between the two sides of the device to allow laminin coating to pass through the microgrooves and the devices were incubated overnight at 37°C in 5% CO_2. Overnight incubation hardened the silicone SND75 devices and further sealed them onto the Aclar sheets. The following day, devices were carefully flushed once with DPBS before plating neural progenitor cells (NPCs).

Differentiation of iPSCs into motor neuronal progenitor cells and seeding in microfluidic device

In brief, iPSCs were harvested using collagenase type IV (Cat N° 10780004) and collected in Corning® ultra-low attachment flasks (Sigma, Cat N° 734-4140) to facilitate embryoid body formation. Cells were maintained in neuronal medium (50% DMEM/F12 (Cat N° 11330032) and 50% Neurobasal medium (Cat N° 21103049) with 0.5% L-glutamine (Cat N° 25030-024), 1% penicillin/streptomycin (Cat N° 15070063), 1% N-2 supplement (Cat N° 17502-048), 2% B-27™ without vitamin A (Cat N° 12587-010), 0.5 µM ascorbic acid (Sigma, Cat N° A4403), and 0.1% β-mercaptoethanol (Cat N° 31350010)) supplemented with 5 µM Y-27632 (Merck Millipore, Burlington, MA, USA; Cat N° 688001), 0.2 µM LDN-193189 (Stemgent, Beltsville, MA, USA; Cat N° 04-0074-02), 40 µM SB431542 (Tocris Bioscience, Bristol, UK, Cat N° 1614) and 3 µM CHIR99021 (Tocris Bioscience, Cat N° 4423) for 2 days with medium changes every day (=day 0-1). The following day (=day 2), neuronal medium was supplemented with 0.1 µM retinoic acid (Sigma; Cat N° R2625) and 500 nM smoothened agonist (Merck Millipore; Cat N° 566660), which was refreshed at day four. On day 7, 10 ng/ml BDNF (Peprotech, Rocky Hill, NJ, USA, Cat N° 450-02B) and 10 ng/ml GDNF (Peprotech, Cat N° 450-10B) was additionally added to the day four medium. On day 9, 20 µM DAPT (Tocris Bioscience, Cat N° 2634) was additionally supplemented to day 7 medium. On day 10, embryoid bodies were dissociated into a single cell NPC suspension using 0.05% trypsin (Gibco, Gaithersburg, MA, USA, Cat N° 25300054) and cryopreserved. NPCs were seeded in the two wells and channel on one side of the microfluidic device at 125,000 cells in 30-50 µl day nine medium supplemented with 1% RevitaCell™ (Cat N° A2644501) per well (total of 250,000

NPCs/device). After seeding, devices were incubated for 5-10 min at 37°C and 5% CO_2 to allow cell attachment to the surface before additional day nine medium was added to all 4 wells for a total of 200 µl/well. Subsequently, 5-6 ml sterile DPBS was added to the 10 cm petri dish around the devices to avoid medium evaporation. Seeding in both wells and channel facilitated a larger and more robust network of MNs, which was less likely to detach during medium changes.

Derivation and maintenance of human mesoangioblasts

Briefly, upon receipt of skeletal muscle biopsy, the tissue was minced and incubated for 2 weeks on collagen from calf skin-coated (Cat N° 17104019) 6-cm dishes in growth medium: 15% FBS (Cat N° 10270106), 1% sodium pyruvate (Life Technologies, Carlsbad, CA, USA, Cat N° 11360-070), 1% non-essential amino acids (Cat N° 11140050), 1% L-glutamine (Cat N° 25030-024), and 0.5% penicillin-streptomycin (Cat N° 15070063), and 1% insulin transferrin selenium (Cat N° 41400045) in IMDM (Cat N° 12440053) supplemented with 5 ng/ml recombinant human basic fibroblast growth factor (bFGF) (Peprotech, Cat N° 100-18B). Medium was changed every 4 days. After 14 days, cells were fluorescent activated cell (FACS)-sorted for human alkaline phosphatase (R&D systems, Minneapolis, MN, USA, Cat N° MAB1448) and expanded further in T75 flasks (Sigma, Cat N° CLS3276) on collagen from calf skin (Cat N° 17104019) in growth medium. Cells were cryopreserved in knockout serum replacement (Cat N° 10828-028) with 10% DMSO (Sigma, Cat N° D2650-100ML), passaged, or seeded in devices when reaching 70% confluence. For passaging MABs were washed once with DPBS, followed by incubation with TrypLE express (Cat N° 12605010) for 3 min at 37°C in 5% CO_2. After incubation, TrypLE was neutralized with growth medium, and cells were gently scraped, collected and centrifuged for 3 min at 0.3 RCF, before cells were counted and reseeded in a T75 or T175 flask or device. Passaging was performed 1-2 times a week for cell expansion until a maximum passage number of 13. Since physical contact between MABs initiates fusion and lowers the myogenic potential, a cell confluence of 70% was never exceeded.

Co-culturing myotubes and motor neurons in microfluidic device

On day 11 of motor neuron differentiation, day 10 medium was refreshed on both sides of the device keeping an equal volume across microgrooves. On day 14, 200 µl neuronal medium supplemented with 10 ng/ml BDNF, 10 ng/ml GDNF and 20 µM DAPT was added to each well to initiate NPC differentiation into spinal MNs (sMNs). On day 16, 200 µl day 14 medium additionally supplemented with 10 ng/ml CNTF (Peprotech, Cat N° 450-13B) was added to each of the four wells. On day 17, MABs were dissociated using TrypLE and seeded in the two wells and channel opposite to the MNs in the microfluidic device at 100,000 cells in 30-50 µl growth medium per well (total of 200,000 MABs/device). After seeding, devices were incubated for 5-10 min at 37°C in 5% CO_2 to allow cell attachment to the surface before additional growth medium was added to the two wells for a total of 200 µl/well. MABs were large cells with spherical morphology when dissociated in suspension. On day 18, MN compartments received neuronal medium supplemented with 10 ng/ml BDNF, GDNF and CNTF, while MABs differentiation into myotubes was initiated in the opposite compartments using MAB differentiation medium containing 2% horse serum (Cat N° 16050122) and 1% sodium pyruvate in DMEM/F12 supplemented with 0.01 µg/ml recombinant human agrin protein (R&D Systems, Cat N° 6624-AG-050). At day 21, a 300% chemotactic growth factor gradient and 200% volumetric gradient were established to facilitate polarized axonal growth through the microgrooves of the microfluidic device towards the myotube compartment. MN compartments received 100 µl/well neuronal medium without neurotrophic factor supplements, while myotube compartments received 200 µl/well neuronal medium supplemented with 30 ng/ml BDNF, GDNF and CNTF in addition to 20 µg/ml laminin and 0.01 µg/ml agrin. The growth factor and volume gradients including laminin and agrin supplements were kept at each medium change, which was performed every other day until day 28 of MN differentiation equivalent to 10 days of co-culturing MNs and myotubes. A spontaneous crossing of neurites from the MN soma compartment towards the myotube compartment without implementation of the chemotactic and volumetric gradient is generally observed. However, with the gradient the amount of neurites crossing and the speed of which this happens are increased.

Tubastatin A treatment

For neurite outgrowth and NMJ quantifications, *FUS*-ALS and isogenic control co-cultures in XC150 devices were treated for 24 h with 1 µM Tubastatin A (TubA) (Selleckchem, Houston, TX, USA, Cat N° S8049) in day 21 medium in combination with the start of the chemotactic and volumetric gradient. TubA was added to both the soma and the myotube compartment. Control co-culture devices were kept in parallel without TubA treatment. At day 28, devices were analysed for neurite outgrowth and NMJ were quantified.

For neurite regrowth, *FUS*-ALS and isogenic control MNs were treated with 1µM TubA in both compartments for 24 h before (pre-axotomy) or for 24 h after (post-axotomy) performing the axotomy. Control devices were kept in parallel without TubA treatment.
For MN FUS-mislocalisation experiments, MNs were plated in 24-well plates (Greiner bio-one cellstar, Vilvoorde, Belgium, Cat N° 662160) and treated with 1µM TubA for 24 h from day 21-22, before subsequent fixation and analysis. Untreated controls were kept in parallel.

Immunocytochemistry
Xona™ XC150 devices were used for immunocytochemistry (ICC) analysis of NMJ formation and neurite outgrowth, while MN differentiation verification, myotube fusion and MN FUS-mislocalisation were imaged on 13 mm #1.5 coverslips (VWR, Monroeville, PA, USA, Cat N° 631-0150P) and in 96-well black tissue culture plates (Perkin Elmer, Waltham, MA, USA, Cat N° 6005430). Cells were washed once with DPBS before fixation using 2-4% paraformaldehyde (Cat N° 28908) for 15-20 min at room temperature (RT). After fixation, cells were permeabilized for 20 min at RT with DPBS + 0.1% Triton X-100 (Sigma, Cat N° T8787-250ML) followed by blocking for 20 min at RT in 5% normal donkey serum (Sigma, Cat N° D9663-10ML) in 0.1% PBS-Triton X-100. Primary antibodies (table S1) were diluted in 0.1% PBS-Triton X-100 with 2% normal donkey serum and incubated with a volume gradient between MN/myotube compartments overnight at 4°C.
The following day, cells were carefully washed and incubated with secondary antibodies (table S2) diluted in 2% normal donkey serum in 0.1% PBS/Triton X-100 for 1h at RT in the dark with a volume gradient between compartments.
To label nuclei, cells were incubated with DAPI (NucBlue Live Cell Stain ReadyProbes reagent, Cat N° R37605) for 20 min and coverslips were mounted with Fluorescence Mounting Medium (Dako, Glostrup, Denmark, Cat N° S3023), while wells in the device were sealed with one drop of mounting medium per well before acquiring images. Coverslips, plates and devices were imaged using an inverted Leica SP8 DMI8 confocal microscope and quantifications were performed utilizing Image J 1.52b software.
For MN quantifications, a minimum of 100 cells were randomly selected based on positive DAPI staining. Five random images at 20x magnification were acquired from each biological replicate. For myotube fusion index, nuclei were counted using Image J particle analyser tool with a nucleus size between 50-700 μm^2. Five random images at 10x magnification were acquired from each biological replicate from each condition. For AChR cluster quantifications, a minimum of 20 random field of visions (=581.8 μm^2) per condition were selected and myotubes was determined based on positive myosin heavy chain (MyHC) marker. MyHC-positive cells containing multiple nuclei were selected as myotubes. For NMJ quantifications, each image field was selected based on α-bungarotoxin (Btx)-positive clustering, recorded in z-stack, and the number of co-localizations between synaptophysin (SYP) and Btx was counted per myotube. For quantifying FUS-mislocalisation in MNs, eight random images at 12-bit and 40x magnification were taken blinded from two technical replicates from each biological replicate per condition. Images were converted to maximum intensity projection, and the nucleus/cytoplasmic ratio of FUS was quantified using a customised automatic Nikon software script.

Scanning electron microscopy
For SEM, myotubes and motor neurons were cultured in Xona SND75 devices on Aclar sheets and fixed with 2.5% glutaraldehyde in 0.1 M Na-cacodylate buffer pH 7.2 for 2 h at RT. After three washing steps in the same buffer, the microfluidic devices were carefully removed and Aclar sheets were clipped to round discs of 18 mm diameter. Subsequently, the discs were incubated in 1% osmium tetroxide for 1 h, washed in milli-Q water and dehydrated in a graded ethanol series to 100% ethanol. The discs were then inserted in a coverslip-holder for critical point drying in a Leica CPD300 apparatus for two hours, in which they were kept submerged in 100% ethanol at all times. Finally, the dried discs were mounted on SEM support stubs with carbon-stickers and coated with 4 nm Chromium in a Leica ACE600 coating machine. Cells and myotubes were studied and imaged in a Zeiss Sigma SEM at an accelerating voltage of 5 kV and at a working distance of 7 mm.

Neurite axotomy and regrowth
FUS-ALS and isogenic control MNs were cultured without myotubes in XC150 devices until day 22 according to our protocol. On day 22, the myotube compartment containing neurites was repeatedly washed from both channel openings with at least 2 ml DPBS and removed using suction in order to mechanically axotomize the neurites (4,5). This was followed by a 15 sec incubation with 100 µl of lysis buffer (2% Triton X-100 (Sigma, Cat N° T8787-250ML) in DPBS) in order to chemically dissolve the remaining tissue. A volume difference between compartments with a higher volume on the MN soma side was maintained during the entire axotomy procedure to minimize the flow back of lysis buffer through the grooves. Afterwards, the lysis buffer was removed and the compartment was again repeatedly washed with DPBS before adding fresh MN medium to

the entire device and restoring the chemotactic and volumetric gradient. Devices were fixed at day 23 to allow the neurites to regrow for 24 h.

Neurite outgrowth and regrowth quantifications

The co-cultures used for NMJ quantification were likewise used for neurite outgrowth quantifications. In addition, MNs cultured in devices without myotubes were used to assess a potential myotube influence on neurite outgrowth as well as assess neurite regrowth upon axotomy. Tile scan images of NEFH fluorescence were taken at 10x magnification in a 1024x1024 format using an inverted Leica SP8 DMI8 confocal microscope. Tile scans were merged automatically using Leica software auto merge and auto stitching with a smooth overlap and linear blending. Afterwards, images were cropped at the microgroove edge displaying solely the myotube compartment with crossing neurites. Neurites were identified and isolated using ilastik 1.3.3post1 Pixel Classification software with a sigma of 0.3-1.6 for color/intensity, edge and texture. The outlined neurites were exported as probabilities predictions. Each image was adjusted for a threshold between 15-70 % (see table S3 and table S4 for exact values) and converted to an 8-bit mask using Image J 1.52p software. Using Image J software's particle remover plugin, pixels between 0-10 μm^2 were removed. To assess neurite outgrowth and regrowth, total number of pixel intersections were quantified utilizing a custom-made Image J 1.52p software script. The script performs a linear Scholl analysis and automatically quantifies the amount of pixel crossings per line intersection similar to a previously published method (6). The distance between each line intersection is 50µm. Due to high neurite density and bundle formation at the exit of the microgrooves, we omitted the measurements at the first line at 50 µm and started measuring at 100µm distance from the microgrooves.

For MN-NPC neurite outgrowth quantifications in mono-cultures, day 10 NPCs were plated in 24-well plates and imaged for 24 h using an IncuCyte ZOOM device with the IncuCyte ZOOM 2016A software and a Nikon S Plan Fluor ELWD 20X/0.45 OFN22 DIC N1 objective (Essen BioScience). Nine images per condition were taken every two hours. Cells were treated with 1-3 µM TubA for 24 h with control conditions receiving no treatment. Neurite outgrowth was analysed using the IncuCyte NeuroTrack Phase Neurites software with a brightness segmentation mode, a segmentation adjustment of 1, a cleanup min cell width of 10 µm, a neurite sensitivity of 0.5 µm and neurite width of 1 µm. The experiment was performed in three independent replicates with two technical replicates in each.

Calcium fluorescent imaging

Xona^{TM} XC150 devices were used for live-cell functionality assessment of NMJs. On day 28 of MN differentiation, myotube compartments were incubated for 25 min at 37°C, 5% CO_2 with 200 µl/well neuronal medium supplemented with 30 ng/ml BDNF, GDNF and CNTF and 5 µM Fluo-4 AM (Cat N° F14201) diluted in Pluronic F-127 (Cat N° P3000MP), while MN compartments received a medium change with 200 µl/well neuronal medium without neurotrophic factors. Fluo-4 AM is a Ca^{2+} indicator, which exhibits an increase in fluorescence upon Ca^{2+} binding. After incubation, the medium was refreshed on both sides in order to re-establish the volume and growth factor gradient. MNs were stimulated with 50 mM potassium chloride (KCl) in neuronal medium and the consequent Fluo-4 fluorescence was recorded in the myotube compartment (10x magnification with 1 s intervals for a duration of 1 min per set). Each field of vision was selected with bright field based on the presence of myotubes in the myotube compartment. For each device, the motor neuron stimulation was performed twice with approximately 2 min pause in between, followed by a positive test of myotube activity with direct stimulation of myotubes with 50 mM KCl in myotube compartment. MN compartment was stimulated once to confirm fluidic isolation and absence of Fluo-4 AM flow back through microgrooves during incubation. In addition, myotubes were cultured without MNs in 24-well black ibitreat µ-plates (Ibidi, Planegg, Germany, Cat N° 82406) and tested for Ca^{2+} functionality, as well as in devices without MNs to confirm fluidic isolation upon KCl stimulation in the MN compartment. To guarantee the specificity of our experiment, myotube compartments were treated with 19 µM of the AChR competitive antagonist tubocurarine hydrochloride pentahydrate (DTC) (Sigma, Cat N° T2379-100G) 10 min before analysis. All recordings were acquired and analysed with a Nikon A1R confocal microscope and NIS-Elements AR 4.30.02 software. For functionality quantifications, each myotube was manually circled utilising NIS-elements Time Measurement tool and individually analysed for increase in Fluo-4 fluorescent signal over a 1-min time period. Increase in Ca^{2+} intensity was calculated as difference between peak value within first 30 recorded seconds and baseline. Baseline was calculated as average value of the first 5 seconds of recordings before KCl stimulation.

Statistics

A biological replicate represents an independent MN differentiation from day 0 to day 28, and independent MAB differentiation into myotubes or an independent co-culture in a device. MN, myotube fusion index and AChR cluster quantifications were performed in three biological replicates, and NMJ quantifications in a total of four replicates with two technical replicates in each. NMJ functionality experiments were performed in four independent co-culture replicates and each experiment was performed in three technical replicates. NMJ blocking experiments with DTC were performed in three replicates. Neurite outgrowth quantifications were performed in three-four replicates using the healthy control iPSC line. For the *FUS*-iPSC lines, NMJ and neurite outgrowth quantifications were performed in three-eight replicates, and for TubA treatment in three-five replicates. Neurite regrowth and FUS-mislocalisation quantifications were done in three replicates with two technical replicates in each experiment. Outliers (Q=1%) were removed in the FUS-mislocalisation analysis.

Supplemental References

1. Terryn J, Welkenhuysen M, Krylychkina O, Firrincieli A, Andrei A, Reumers V, et al. Topographical guidance of PSC-derived cortical neurons. J Nanomater. 2018;5238901.
2. Guo W, Naujock M, Fumagalli L, Vandoorne T, Baatsen P, Boon R, et al. HDAC6 inhibition reverses axonal transport defects in motor neurons derived from FUS-ALS patients. Nat Commun. 2017;8(1):861.
3. Wang H, Guo W, Mitra J, Hegde PM, Vandoorne T, Eckelmann BJ, et al. Mutant *FUS* causes DNA ligation defects to inhibit oxidative damage repair in Amyotrophic Lateral Sclerosis. Nat Commun. 2018;9:3683.
4. Nijssen J, Aguila J, Hoogstraaten R, Kee N, Hedlund E. Axon-Seq Decodes the Motor Axon Transcriptome and Its Modulation in Response to ALS. Stem Cell Reports. 2018;11:1565–78.
5. Nijssen J, Aguila J, Hedlund E. Axon-seq for in Depth Analysis of the RNA Content of Neuronal Processes. Bio-Protocol. 2019;9(14):1–16.
6. Jocher G, Mannschatz SH, Offterdinger M, Schweigreiter R. Microfluidics of small-population neurons allows for a precise quantification of the peripheral axonal growth state. Front Cell Neurosci. 2018;12:166.